Dissertation

submitted to the

Combined Faculties for the Natural Sciences and for Mathematics

of the Ruperto-Carola University of Heidelberg, Germany

for the degree of

Doctor of Natural Sciences

presented by:

Patric Pelzer, M.Sc. Neuroscience

born in: Bergisch Gladbach, Germany

Oral-examination: ....

A Paleocortico-Thalamo-Cortical Circuit Operating Giant Synapses

Referees: Prof. Dr. Thomas Kuner

     Prof. Dr. Hannah Monyer

Summary

The thalamus is a critical relay station in the pathway for sensory information to the cortex and additionally important for the intercortical information transfer. An exception is the olfactory system, as it does not require a thalamic relay step before the information reaches the cortex. Olfactory receptor neurons send axonal projections to the olfactory bulb, from where the information proceeds to the primary olfactory cortex. It is only from the piriform cortex (PIR) that the information is passed to the prefrontal cortex via direct projections and via the mediodorsal thalamus (MD). Aside the for a sensory system exceptional connectivity, does this circuit also stand out against other cortico-thalamo-cortical loops. The PIR belongs to the paleocortex instead of neocortex, the contributor to most other cortico-thalamo-cortical loops.

This situation raises the question if paleocorticothalamic projections have the same function as their subcorticothalamic or neocorticothalamic equivalents?

In this thesis, I utilize a highly precise spatiotemporal gene transfer system via adeno-associated viruses to label PIR synapses. In acute slice preparations these synapses may be excited individually by juxtapositioned near field simulation electrodes. Based on the kinetics of the evoked postsynaptic currents and immunohistological stainings, I propose glutamate as the principle neurotransmitter. The PIR-MD synapse displays short-term depression, as it has been shown for other thalamic afferences, classified as "drivers".

In an electronmicroscopic preparation the complex dendritic interface of PIR-MD synapses becomes apparent. Often multiple dendritic excrescences invade the presynaptic profile. The presynaptic lumen is filled with vesicles and mitochondria. Altogether the morphology is that of a typical driver synapse in the thalamus.

Surprisingly, I found chemical synapses onto intermediate stretches of labeled axons, a constellation that has not been described in MD or elsewhere previously.

In summary, the results show that the olfactory brain circuit may have an additional level of complexity, imposed by axo-axonal contacts, and that PIR-MD synapses function like driver synapses in other transthalamic projections. However, as the term "driver" suggests that it always evokes postsynaptic action potentials, which is not true for the PIR-MD synapse, the recently proposed term "class I" synapse is adopted.

Zusammenfassung

Der Thalamus ist eine wichtige Zwischenstation sensorischer Informationen auf dem Weg zum Cortex und im intercortikalen Informationsaustausch. Eine Ausnahme ist der Geruchssinn. Er unterscheidet sich in seiner anatomischen Verschaltung von anderen Sinnesmodalitäten insofern, dass die Informationen ohne thalamische Zwischenstation in den Cortex gelangen. Die olfaktorischen Rezeptorneurone bilden Axone zum Bulbus olfactorius aus und von dort werden die Informationen zum olfaktorischen Cortex weiter-verschaltet. Erst vom Cortex piriformis (PIR), dem Großteil des olfaktorischen Cortex, gelangt die Information in den mediodorsalen Thalamus (MD). Neben dieser außer-gewöhnlichen Konnektivität stellt das olfaktorische Netzwerk auch eine Besonderheit unter den cortico-thalamo-corticalen Verbindungen da. Der PIR ist nicht Teil des Neocortex, wie für die meisten andern cortico-thalamo-corticalen Verbindungen, sondern Teil des Paläocortex.

Dies wirft die Frage auf, ob paläocorticothalamische Projektionen ähnlich wie andere subcorticothalamische oder neocorticothalamische Projektionen funktionieren?

In dieser Arbeit nutze ich den zeitlich und lokal präzise definierten Gentransfer via adeno-assoziierten Viren um PIR-MD Synapsen zu markieren. In akuten Hirnschnitten lassen sich diese mittels lokalbegrenzt agierender Elektroden stimulieren. Basierend auf der Kinetik der evozierten postsynaptische Ströme und immunohistologischer Untersuchungen konnte Glutamat als primärer Neurotransmitter ermittelt werden. Während repetitiver Stimulation zeigen die Synapsen eine stark ausgeprägte frequenzabhängige Ermüdung.

Im elektronenmikroskopischen Präparat zeigt sich die aufwendig strukturierte Kontaktfläche zwischen Dendriten und PIR-MD Synapse. Häufig dringen dendritische Auswüchse in die Präsynapse ein. Die Präsynapse ist mit Vesikeln und Mitochondrien gefüllt. Diese Morphologie entspricht der einer typischen thalamischen „Driver"-Synapse.

Überraschenderweise, konnte ich chemische Synapsen direkt auf markierte PIR-Axone nachweisen. Dieser Typ von Synapse wurde für den MD bisher nicht beschrieben. Darüber hinaus wurden axo-axonale Kontakte außerhalb des Axonhügels, zwischen zwei Synapsen oder von elektrischen Synapsen zwischen zwei Axonen auch in anderen Hirnregionen noch nicht beschrieben.

Zusammenfassend zeigen die Ergebnisse, dass das olfaktorische Netzwerk eine zusätzliche Ebene an Komplexität durch einen neuen Typ von axo-axonalen Synapsen erhält und dass PIR-MD Synapsen der Klasse der thalamischen „Driver"-Synapsen angehören. Da der Begriff „Driver" suggeriert, dass immer postsynaptische Aktionspotentiale ausgelöst werden können, dies aber experimentell nicht bestätigt werden kann, wird der kürzlich postulierte Begriff der „class I" Synapsen übernommen.

Table of Contents

1   Introduction

All organisms respond to and interact with their environment. In order to select the most appropriate response for a given situation, the organism must continuously sample the environment with all its senses. Humans differentiate 5 main senses: sight, hearing, touch, taste, and smell. Olfaction, i.e. the sense of smell, is the chemoreception of volatile molecules. The neuronal circuitry processing olfactory information has some peculiarities in comparison with the circuitries of other modalities. Firstly, olfactory information does not route through the thalamus before reaching the cortex (Leinwand and Chalasani, 2011; Sherman and Guillery, 2006). It is only from the primary olfactory cortex, that the information is passed on to secondary cortices via direct projections and indirectly via the thalamus (Datiche and Cattarelli, 1996; Powell et al., 1965). The functional contribution of the thalamic detour is largely unknown (Courtiol and Wilson, 2015). Secondly, as this thalamic afference originates, unlike for most other thalamic nuclei, from a paleocortical area, it offers the opportunity to compare it to other cortical and subcortical afferences, identify communalities, and generalize to all thalamic nuclei.

First, I will describe some general aspects of the thalamus, proceed to olfaction and its processing circuit, and then outline the mediodorsal thalamus and its role in olfaction in more depth.

1.1   Thalamus

The thalamus derives from the diencephalon and locates to the center of the brain, i.e. in short distance from most other brain structures (Dong, 2008). In rodents, unlike in other mammals, the thalamus is almost exclusively made up of relay neurons except for a sheet of inhibitory interneurons, the nucleus reticularis, at its lateral flanks (Arcelli et al., 1997; Kuroda et al., 1992a; Sherman and Guillery, 2006).

Traditionally the thalamus has been described as the gateway to the cortex. It was assumed to be a mere selective information relay hub. However, the notion of a pure gateway is increasingly challenged and the thalamus is recognized as an important processing station involved in various tasks (Sherman and Guillery, 2002, 2006). The nature of the processing depends on the nucleus and its connectivity.

1.1.1   Thalamic Relay Neurons

Thalamic relay neurons constitute the principal output of the thalamus. They are the almost exclusive neuronal cell type in most thalamic nuclei in rodents. Interneurons are reported to make up less than 1 % of all neurons (Arcelli et al., 1997; Kuroda et al., 1992a). Relay neurons use glutamate as the principal neurotransmitter and are therefore excitatory. In

general are these neurons classified as multipolar neurons. Relay neuronal axons usually pass through the nucleus reticularis, the sheet of inhibitory neurons, branch off collaterals and proceed to the neocortex. The axons may in principle terminate in all layers of the neocortex, but usually concentrate on one or two layers in an area specific pattern (Jones, 2009).

Thalamic relay neurons operate in two different firing modes: tonic and burst mode (Llinás and Jahnsen, 1982). The two modes subserve different functions. The burst mode may function as a "wake-up" call, which amplifies unexpected or new stimuli and draws attention (Guido et al., 1995; Sherman, 2001, 2005). Tonically firing neurons allow a more accurate linear rate-coded representation of the stimulus details (Guido et al., 1995; Sherman, 2001, 2005). The burst and tonic mode are also associated with the asleep and awake brain. During sleep the burst mode is more prominent. During wakefulness the tonic activity patterns predominate (Guido and Weyand, 1995; Ramcharan et al., 2000). However both modes may be found in either state, just at different probabilities (Weyand et al., 2001).

The burst mode is mediated by low-voltage activated calcium-channels ($Ca_v3.1$-3.3), also known as T-type calcium-channels (Cain and Snutch, 2013; Sherman, 2005). The channels are closed at membrane resting potential and open transiently upon depolarization. The activation threshold is in a similar range of sodium-channels, close to the membrane resting potential. The calcium influx is strongest at around -30 to -20 mV. The corresponding EPSP usually lasts between 50 and 200 ms and has an amplitude of 20 to 30 mV (Cain and Snutch, 2010; Sherman and Guillery, 2006). As the generic term "spike" may also refer to an action potential, this spike is called the low-threshold spike (LTS) (Suzuki and Rogawski, 1989). Several high frequency action potentials ride on the LTS. The channels inactivate like sodium-channels. Once inactivated the block must be removed by hyperpolarization (Coulter et al., 1989).

The transition between the burst and tonic mode is regulated by the membrane potential (Mease et al., 2014). When hyperpolarized, most channels are deinactivated and ready to open, while they are inactivated at more depolarized potentials. In tonic mode, unlike in burst mode, a single synaptic EPSP evokes not more than a single action potential. Hence, thalamic relay cells transform the information content of the inputs and recode the representation for further processing in the cortex.

1.1.2 Thalamic Excitatory Synapses: Drivers and Modulators

Excitatory synapses in the thalamus split into two groups: drivers and modulators (Sherman and Guillery, 2006). EPSCs evoked by drivers are fast and have high amplitudes. Modulators are slow and less influential. However they control the switch between burst and tonic modes in response to the input of drivers and control spontaneous activity. Modulators cannot evoke an action potential directly.

Although modulators outnumber driver synapses by far, one must not be misled to believe that the nucleus at hand reflects the same functional purpose as the modulator source nucleus (Sherman and Guillery, 2006). The receptive field of the relay neurons is determined

by the driver synapses (Sherman and Guillery, 2006). For example the lateral geniculate nucleus (LGN) relays retinal information, although the directly visually related synapses are outnumbered by synapses from the brainstem (Sherman and Guillery, 2006).

The functional difference between driver and modulators is correlated to some morphological traits. In electron microscopy studies the driver synapses are believed to correspond to cross-sections of large terminals with round vesicles (hence also the abbreviation RL-type). Modulators are assumed to correspond to the RS-type (round vesicles, small terminal) (Sherman and Guillery, 2006). RL-boutons tend to be in closer proximity to the soma than modulators (Kuroda et al., 1992b). This already strengthens the postsynaptic impact as shorter distances in dendrites are less prone to electrotonic signal decay (dendritic filtering). As mentioned above, RL-terminals are, with an average cross-section of 1.05 - 2.15 μm^2, larger than modulators (0.28 - 0.36 μm^2) (Çavdar et al., 2011). Others use the diameter, instead of the area, to differentiate between the RS (<1 μm) and RL-terminals (>2 μm) (Rovó et al., 2012). RL-terminals possess higher numbers of vesicles, active zones and mitochondria (Sherman and Guillery, 2006). The higher number of active zones is again in line with the stronger influence of a driver on the postsynaptic neuron in comparison to the modulators. More active zones do not inevitably require more vesicles, but it seems reasonable to scale the pool with the increased number of vesicle fusions. The bouton lumen also contains multiple mitochondria.

Functionally, driver synapses depress during repetitive high-frequency stimulation, from which they recover within seconds during silence (Groh et al., 2008; Seol and Kuner, 2015; Urra Quiroz, 2014). The kinetics and extend of the short-term depression (STD) depends on the stimulation frequency (Groh et al., 2008; Seol and Kuner, 2015; Urra Quiroz, 2014). Modulators exhibit the opposite short-term plasticity phenotype, i.e. short-term facilitation (Li et al., 2003; Sherman and Guillery, 2006).

The differentiation between driver and modulator extends to the postsynaptic side. Drivers activate fast ionotropic receptors, modulators slower metabotropic glutamate receptors (Seol and Kuner, 2015; Sherman and Guillery, 2006). Currents evoked by metabotropic receptor activation are usually subtle, but long lasting, while ionotropic receptors display faster opening and decay kinetics with larger current amplitudes. The fast decay of the postsynaptic potentials after ionotropic receptor activation restricts the time window, but allows for a finely tuned integration of multiple inputs (Groh et al., 2008).

1.1.3 First-Order and Higher-Order Nuclei of the Thalamus

Thalamic nuclei are grouped in first-order and higher-order nuclei. The separation is based on the source of the principal, i.e. the driving, inputs of the nucleus (Sherman and Guillery, 2006). First-order nuclei receive their driving input from non-cortical structures. Good examples are nuclei like the LGN, the visual nucleus of the thalamus, or the medial geniculate nucleus, the auditory nucleus of the thalamus. The inputs come from non-cortical elements, i.e. the superior and inferior colliculus, which are part of the visual and auditory pathway, respectively. The thalamus in turn, forwards the information into the visual and

auditory cortex. However, first-order nuclei are not spared from cortical input. In fact, the majority of synapses originate from cortical layer VI neurons and other non-cortical areas in form of modulators (Sherman and Guillery, 2006).

Higher-order nuclei receive their driving inputs from neurons residing in the cortex (Sherman and Guillery, 2006). Two examples for such a high-order nucleus are the mediodorsal thalamus (MD) and medial posterior nucleus (POm). The MD in rodents is slightly different from other higher-order nuclei, in the sense that it does not receive its principal input from layer V neocortical neurons, but from paleocortical neurons (Kuroda et al., 1992b; Kuroda and Price, 1991; Ray et al., 1992). Its behavioral context and its connectome will be discussed in more detail below, as this nucleus is essential for this thesis. Higher-order nuclei receive modulatory input from layer VI neurons and other non-cortical areas as well. The relay neurons may either project back to the same cortical area they received input from or serve as an intercortical information transfer station (Sherman and Guillery, 2006).

1.2 Olfaction

An odor consists of a mixture of volatile molecules. The airborne molecules pass the olfactory epithelium with every breath. These molecules dissolve in the mucus and are recognized by the olfactory receptor neurons (ORNs). The detection is transduced into an electric signal and send to the first relay station in the brain - the olfactory bulb (Figure 1.1) (reviewed by Leinwand and Chalasani, 2011). Within the olfactory bulb the signals from the ORNs are integrated and further passed on to the primary olfactory cortex by mitral and tufted cells (Leinwand and Chalasani, 2011). The primary olfactory cortex circumscribes all cortical areas which receive input from the olfactory bulb. These areas are: the anterior olfactory nucleus, the olfactory tubercle, the cortical nucleus of the amygdala, the lateral entorhinal cortex, and, the largest area, the piriform cortex (PIR) (Price, 1973, 1985). The bisynaptic, direct connection to the cortex separates the olfactory circuit from the other senses, which all include one intermediate relay station in the thalamus (Sherman and Guillery, 2006). The PIR communicates with secondary olfactory related cortical areas, like
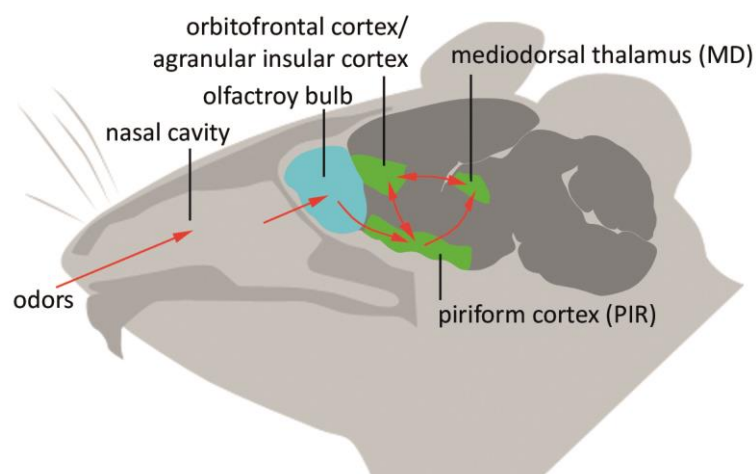
Figure 1.1: **Transduction of Olfactory Stimuli**. Odors reach the nasal cavity, are recognized and the according signals are send to the olfactory bulb. From there the projections go to the primary cortex, here represented by the piriform cortex (PIR). The PIR is reciprocally connected with the orbitofrontal/agranular cortex and the mediodorsal thalamus (MD). The MD is also reciprocally connected to the orbitofrontal/agranular cortex.

the orbitofrontal and agranular insular cortex by strong direct reciprocal connections, and indirectly via the mediodorsal thalamus (MD) (Figure 1.1) (Price and Slotnick, 1983). The MD also has a strong reciprocal connection with the orbitofrontal and agranular insular cortices (Kuroda et al., 1993a).

1.3   Mediodorsal Thalamus

The mediodorsal thalamus (MD) is a higher-order nucleus close to the dorsal edge of the thalamus and the bilateral nuclei are separated at the midline of the brain by only a thin sheet of neurons - the intralaminar and the paraventricular nuclei. The MD can be divided in three subareas: lateral (MDl), central (MDc), and medial (MDm) (Groenewegen, 1988; Krettek and Price, 1977; Kuroda et al., 1998). The subdivision is based on the respective connectome and additionally the dendrites seldom cross the border (Kuroda et al., 1998).

Kuroda and colleagues (1992a, 1998) claim to have identified two cell types in the MD: stellate and fusiform neurons. They segregated neurons to either cell type based on size and the dendritic structure. Stellate cells are medium sized neurons (25 - 31 μm by 18 - 23 μm) and have 4 to 8 primary dendrites. The primary dendrites branch into 2 to 3 secondary branches within 5 - 30 μm from the soma. The dendritic tree spans a sphere around the soma. Fusiform cells are slightly smaller (23 - 29 μm by 16 - 21 μm). The soma has 3 to 5 primary dendrites, which split into 2 - 3 secondary dendrites within a short distance. The dendritic tree is relatively sparse compared to the stellate cells. They however acknowledge that there are intermediate neurons and a classification is not always possible.

The MD receives input from a variety of different structures, including but not restricted to the piriform cortex (PIR), prefrontal cortex, amygdala, parts of the basal ganglia (including ventral pallidum), hypothalamus, and entorhinal cortex. As this study focuses on the olfactory aspects of the MD only these connections will be briefly reviewed. The PIR, the major part of the olfactory cortex, and its associated deep layer, the endopiriform cortex, send projections to MDc and MDm. The terminals have been shown to be mainly RL-boutons and with a small contribution of some RS-terminals (Kuroda et al., 1992b; Kuroda and Price, 1991). The density of occurrence is highest on primary, then secondary, tertiary and finally higher-order dendrites (Kuroda et al., 1992b). The neurotransmitter is not unequivocally determined. Some cells can be labelled by ^{3}H-D-aspartate, indicating that these neurons are glutamatergic. A possibly different subsection of piriform corticothalamic neurons are also immunoreactive for neurotensin (Kuroda et al., 1991; Ray and Price, 1990). No GABAergic piriform corticothalamic connections have been reported (Ray et al., 1992; Young et al., 1984). The connection from PIR to MD is unidirectional and no feedback from the MD interacts with PIR neurons. The MD relay neurons project to the prefrontal cortex (PFC). The projection to the orbitofrontal and agranular insular parts of the prefrontal cortex is of particular interest, as these also receive direct input from the PIR. The connection between the PFC and MD is monosynaptically reciprocal (Kuroda et al., 1993a). Cortical neurons projecting to MD are situated in layer V and VI (Kuroda et al., 1993a). Layer VI neurons are supposed to form modulatory synapses in the thalamus, while layer V gives rise to drivers

(Sherman and Guillery, 2006). Interestingly, RL-type synapses from the PFC have been found in the MD of cats and monkeys (Kuroda et al., 1993b; Schwartz et al., 1991), but not in rats or mice, although layer V neurons project to the MD across all species (Kuroda et al., 1993b, 1998; Mátyás et al., 2014; Schwartz et al., 1991). The cortiothalamic projection neurons to the MD and are probably glutamatergic (Ray et al., 1992). Kuroda et al. (1992b) described the PIR as the only source of RL-type synapses in in the central part of the MD.

1.3.1 Olfaction in the Mediodorsal Thalamus

There is good evidence that olfactory related information is processed in the MD. However, most MD related research focuses on its executive function in learning and behavioral flexibility in line with the dense reciprocal connection with the prefrontal cortex.

The first line of evidence that the MD is involved in olfaction stems from electric stimulation of the olfactory tract or olfactory bulb. The stimulation evokes short latency activity in the MD of rats (Inokuchi et al., 1993; Price, 1985; Price and Slotnick, 1983). Similar results are available for monkeys and rabbits (reviewed by Courtiol and Wilson, 2015). Data, obtained from single-unit recordings while stimulating with odorants in the anesthetized animal, further supports this notion (Courtiol and Wilson, 2013). This study revealed that 51 % of all recorded MD units were odor-responsive. The units were narrowly tuned, i.e. they responded to only a single component of the tested odor sets. This may be attributed to the anesthesia or be species specific (rat), as two other studies found that MD neurons in rabbits and monkeys responded to multiple odors (Imamura et al., 1984; Yarita et al., 1980). Courtiol and Wilson also showed that some MD unit's activity was phase-locked to the respiratory cycle (Courtiol and Wilson, 2013). Moreover, some MD neurons fire in phase with the beta oscillation in the PIR (Courtiol and Wilson, 2013).

Even though the above mentioned studies prove that olfactory related information is processed in the MD, they do not allow speculation on its nature. Lesion studies show that animals lacking a functional MD do not turn anosomic, i.e. unable to smell (Eichenbaum et al., 1980; Slotnick and Kaneko, 1981; Staubli et al., 1987), but exhibit behavioral alterations in odor discrimination, reversal learning, and emotional value association (Rousseaux et al., 1996; Sapolsky and Eichenbaum, 1980; Slotnick and Kaneko, 1981; Slotnick and Risser, 1990). Slotnick and Risser (1990) showed that MD lesioned rats need, at least for the first two odor sets of a 2-oder discrimination task, more trials to criterion than control rats. Furthermore, these animals performed worse during reversal learning tasks. Staubli et al. (1987) found similar deficits in odor discrimination. Here, the performance of control animals got better with consecutive odor pairs, while lesioned rats performed on constant level, such that the difference between the two groups increased with each new odor pair.

Also in humans there is evidence for a thalamic contribution to olfactory processing. Plailly et al. (2008) showed that the BOLD-signal in MD does not show an activation in classical fMRI analysis, but the effective connectivity increased between PIR to MD and MD to PFC, selectively, during odor attention tasks. Furthermore, Tham et al. (2011) could show that

patients with a lesion of the mediodorsal thalamus perform poorer on an odor-attention task than healthy controls.

In conclusion, the MD may be involved in regulation of attention to olfaction, odor short-term memory, participate in the integration of odor and hedonic value from the amygdala, or other associative learning.

1.3.2   Non-Olfactory Functions of the Mediodorsal Thalamus

Besides its role in olfactory processing the MD is involved in a variety of cognitive tasks as recently reviewed by Mitchel and Chakraborty (2013). The list of behavioral deficits found in various lesion studies, includes short-term memory impairments, deficits in associative learning, and deficits in behavioral flexibility.

1.4   Aim of the Study

The main goal of this project was to quantitatively describe the potential driver synapses between the PIR and the MD. Are they, from an electrophysiological point of view, the same or different from other non-paleocorticothalamic drivers? Do they differ in respect of their ultrastructure? Could the transthalamic olfactory information route be the neuronal substrate for attention?

Driven by these questions, I evaluated the synaptic transmission properties of the PIR-MD synapse in a single synapse stimulation paradigm. Additionally, I investigated the ultra-structure of this synapse and its surrounding tissue by electron microscopy.

2 Material & Methods

2.1 Mice

All C57Bl/6 mice were ordered as mothers plus litter (5 to 6 pups) from Charles River. They were kept at standard housing condition on a 12h-12h day-night cycle. Mice had *ad libitum* access to food and water.

2.2 Plasmids

2.2.1.1 pAM-SyPhy-eGFP / pAM-SyPhy-mCherry / pAM-SyPhy-2-pHluorin

The cDNAs of the fluorescent proteins (enhanced GFP (eGFP), mCherry, and two repeats of pHluorin (2-pHluorin)) coupled to synaptophysin (SyPhy) were subcloned into the pAM vector backbone. The backbone consists of the 1.1 kb long joint cytomegalovirus enhancer sequence and chicken β-actin promoter, the woodchuck post-transcriptional regulatory element and the bovine growth hormone polyA signal. SyPhy-2-pHluorin contains two copies of pHluorin, a pH sensitive variation of GFP and a strong reactive oxygen donor (Horstmann et al., 2013).

2.3 Adeno-Associated Virus Production

Adeno-associated virus (AAV) particles were produced in HEK293 (293AAV, Agilent Technologies, Santa Clara, CA, USA) cell cultures. 4×10^6 HEK cells were seeded in DMEM (PAN-Biotech, Aidenbach, Germany), supplemented with 10 % fetal calve serum (FCS), 0.2 mM non-essential amino acids, 2 mM Na-pyruvate, and 1 % penicillin/ streptomycin on a 14 cm cell culture dish. The desired AAV was a chimera between the serotypes 1 and 2. The serotypes differ by their capsids, for which the DNA is provided by the plasmids pDP1rs and pDP2rs, respectively. After 24 h the cells were transfected with equimolar amounts of pAM plasmids, pDP1rs, and pDP2rs using the calcium phosphate precipitation method. The transfection mixture for a single dish was composed of: 125 mM $CaCl_2$ and 37.5 µg DNA in 2 mL HBS (in mM: 140 NaCl, 25 HEPES, 0.7 Na_2HPO_4, pH 7.05). It was applied in drops to the dish to yield a total of 22 mL. The medium was replaced after 24 h. Three days after transfection a crude cell lysate was collected, from which viral particles were purified. Therefore cells were removed from the dish, pelleted (200 g, 10 min), resuspended in lysis buffer (in mM: 150 NaCl, 50 Tris-HCl, pH 8.5), and lysed via three freeze/thaw cycles. Contaminating genomic DNA was digested with 50 U of benzonase endonuclease (Sigma-Aldrich, St. Louis, MO, USA) for 2 h at 37 °C. Cell debris was removed by pelleting (195 g, 15 min) and the supernatant was passed through a 0.45 µm pore-size filter to yield the crude lysate. AAV particles were purified from this crude lysate by affinity chromatography in a heparin-agarose Typ I column (Cat. No: 7321010, Biorad, Hercules, CA, USA). Columns were

prewashed with 10 mL equilibration buffer (in mM: 1 MgCl$_2$, 2.5 KCl in PBS, pH 7.2). The column was activated first by 5 mL heparin-agarose (Cat. No: H6508, Sigma-Aldrich) and then 10 mL equilibration buffer. Once the heparin-agarose had settled the equilibration buffer was drained. The crude lysate was applied to the column and incubated for 2 h at 4 °C on a shaker. The non-bound components were drained and the column rinsed with 20 mL equilibration buffer. The viral particles were eluted with 15 mL elution buffer (in mM: 500 NaCl, 50 Tris-HCl, pH 7.2) and collected in a filter tube (Cat. No: UFC9 100 24, Amicon Ultra Filter, Merck Millipore, Darmstadt, Germany). The liquid phase of the eluate was removed from the tube by centrifugation (3645 g). When less than 1 mL remained (typically <3 h), the tube was washed with 15 mL PBS followed by centrifugation for three times. The last centrifugation step reduced the volume down to less than 200 μL. This virus stock solution was filtered (0.22 μm pore diameter) one last time, aliquoted, and stored 4 °C.

2.4 Stereotaxic-Guided Virus-Infusion

All injections were performed using a stereotaxic alignment system (basic model: 1900, David Kopf Instruments, Tujunga, CA, USA). Mice (P 14) received an initial anesthesia with 5 % isoflurane in O$_2$ carrier gas (Vaporizer: Isotec4, Surgivet, Dublin, OH, USA). To ensure analgesia after the surgery, mice were subcutaneously injected with Carprofen (10 mg/kg body weight, product name: Rimadyl, Pfizer, Berlin, Germany), preheated to 37 °C. A lack of reflexes to usually painful stimuli (pinch between the toes and in the tail) indicated an adequate anesthesia and analgesia. The fur on the head was trimmed, lose hairs were blown way, and the skin was disinfected with 70 % ethanol. Lidocain (product name: Xylocain 1 %, AstraZeneca, Wedel, Germany), preheaded on a 37 °C plate and injected subcutaneously, ensured additionally local anasthesia. Then the head was fixed in the stereotaxic frame. The skin on the head was cut and the connective tissue was removed as necessary. From now onwards the anesthesia was maintained with 1.5 % isoflurane. Throughout the surgery the skull and tissue was repetitively moistened with ringer solution (in mM: 135 NaCl, 5.4 KCl, 5 HEPES, 1.8 CaCl$_2$, 1 MgCl$_2$). To protect the eye from dehydration, Bepanthen (Bayer, Leverkusen, Germany) was used to cover them. After application of the eye protective, the skull was leveled according to the coordinate system of Allen Reference Atlas (Dong, 2008) using the eLeVeLeR (Sigmann Elektronik, Hüffenhardt, Germany) device. Upon leveling craniectomies were performed with a dental drill (EXL-40, Osada, Los Angeles, CA, USA) at the appropriate coordinates. Injection needles, pulled from micropipettes (Cat. No: 708707, Brand, Wertheim, Germany) on a horizontal puller (P97, Sutter Instruments, Novato, CA, USA), were filled with the virus. The virus was therefore sucked into the needle by negative pressure. Alternatively, the Nanoject II (Drummond Scientific Company, Broomall, PA, USA) was loaded with the virus. The virus was injected into the brain at the appropriate sites (Table 2.1 and Table 2.2), either by manually applied slight positive pressure or by using the Nanoject II. After the injection the incision was sutured. The whole procedure lasted between 30 and 60 minutes. After end of isoflurane administration they recovered within minutes and could be returned to their home cage.

Table 2.1: **Initial Stereotaxic Coordinates to Target the Piriform Cortex in P14 mice.** Coordinates are adjusted from the Allen Reference Atlas. The z drive was angled at 27°. Z-axis ranges indicate the beginning and end of trajectories with continuous release of virus particles.

X	Y	Z	Volume (nL)
3.5	2.3	4.7	25 - 50
4.1	1.9	4.7 - 5.0	50 - 100
4.8	1.5	4.8 - 5.1	50 - 100
5.0	1.5	4.9	25 - 50
4.9	1.1	4.8 - 5.1	50 - 100
5.1	1.1	4.9	25 - 50
5.0	0.7	4.8 - 5.1	50 - 100
5.2	0.7	4.9	25 - 50

Table 2.2: **Final stereotaxic coordinates to target the piriform cortex in P14 mice.** Coordinates are adjusted from the Allen Reference Atlas. The z drive was angled at 27°. Z-axis ranges indicate the beginning and end of trajectories with continuous release of virus particles by the Nanoject II.

X	Y	Z	Volume (nL)
3.3	2.3	4.7	6x 4.6
3.7	2.1	4.7	3x 4.6
4.1	1.9	4.7 - 5.0	6x 4.6
4.5	1.7	5.0	3x 4.6
4.9	1.5	4.8 - 5.1	6x 4.6
5.0	1.1	4.8 - 5.1	6x 4.6
5.1	0.7	4.8 - 5.1	6x 4.6

During the initial two post-surgery days, the analgesia was maintained with additional, daily Carprofen injections.

2.5   Leica TCS SP5 Microscope

A Leica TCS SP5 equipped with an epifluorescence & transmission light path and a confocal mode was used. For electrophysiological experiments the microscope was set up with a HCX APO 20x/1.00 W objective, for fixed tissue imaging with an HCX PL APO 63x1.30 GLYC (ne = 1.451) CORR CS objective. Light transmission microscope images were acquired with a DFC 360 FX camera controlled by the Leica Software (LAS AF v2.2.1, Leica Microsystems). The tissue was contrasted with a Dodt-tube illumination (Luigs & Neumann, Ratingen, Germany). In confocal mode the photons were detected with photomultipliers.

For electrophysiological recordings a HEKA EPC-10 amplifier (HEKA Electronics, Lambrecht, Germany), controlled by PatchMaster (v2.73x1, HEKA Electronics), was used. The stage and electrodes were controlled with micromanipulators from Luigs & Neumann.

2.6 Electrophysiology

2.6.1 Acute Slicing

Acute slices were prepared the earliest at 12, the latest at 37 days post-surgery. Mice were decapitated and the head was dropped into an ice-cold slicing solution (in mM: 85 NaCl, 2.5 KCl, 10 glucose, 75 sucrose, 25 $NaHCO_3$, 1.25 NaH_2PO_4, 3 $MgCl_2$, 0.1 $CaCl_2$, 3 3-myo-inositol, 2 Na-pyruvate, 0.4 ascorbic acid, aerated with carbogen (5 % CO_2), pH 7.3). The skin and the dorsal skull were cut and removed, until finally the brain could be taken out. It was placed in fresh ice-cold slicing solution. This procedure was performed as fast as possible to ensure a low rate of cell death. The posterior part was cut off slightly before the border the cortex and cerebellum. The anterior brain was glued on the flat surface of the cutting edge to the tissue holder of the vibratome (VT1200 S, Leica, Germany). The slices were cut with the following parameters: 250 - 300 µm sections, 0.08 mm/s forward advancement, 50 Hz, and 1 mm amplitude. The anterior pole was either disposed or fixed in 4 % PFA (overnight or longer). Slices containing the MD were transferred to the slice holding chamber with incubation solution (in mM: 109 NaCl, 4 KCl, 35 glucose, 25 $NaHCO_3$, 1.25 NaH_2PO_4, 1.3 $MgCl_2$, 1.5 $CaCl_2$, 3 3-myo-inositol, 2 Na-pyruvate, 0.4 ascoribic acid, aerated with carbogen, pH 7.3) at 37 °C for at least 30 minutes.

2.6.2 Electrophysiological Recordings

Whole-cell patch-clamp recordings were established from mediodorsal thalamus neurons. All neuros were recorded at room temperature (22 ± 1 °C) in artificial cerebrospinal fluid (ACSF, in mM: 125 NaCl, 2.5 KCl, 15 glucose, 25 $NaHCO_3$, 15 NaH_2PO_4, 2 $CaCl_2$, 1 $MgCl_2$, aerated with carbogen, pH 7.3). The patch electrodes were pulled from borosilicate glass capillaries (1B150F-4, World Precision Instruments, Sarasota, Florida, USA) on a horizontal puller (P97, Sutter Instruments, Novato, CA, USA) and had an open tip resistance of 3 - 7 MΩ. They were backfilled with intracellular solution (in mM): 130 K-gluconate, 20 KCl, 5 Na_2phosphocratine, 10 HEPES, 5 EGTA, 4 Mg-ATP supplemented with Alexa 594 (37 µM and additional 0.73 mM KCl; life technologies, Carlsbad, CA, USA). For some measurements 16 mM KCl was replaced by K-gluconate.

Labeled synapses were identified either in confocal or epifluorescent mode and nearby cells were patched in whole-cell mode. The visually-guided approach of the patch electrode to the neuron was aided by the scanning gradient-contrast as previous described elsewhere (Groh et al., 2008; Seol and Kuner, 2015). The intracellular solution was supplemented with Alexa 594, thus the dendritic tree could be imaged after the cytosol and electrode solution equilibrated. Synapses close to a dendrite were tested on their connection to the patched neuron by juxtapositing of a stimulation electrode. The stimulation electrode was obtained from a Theta-Bo-glasscapillary with a tip opening of 1 to 2 µm (Cat. No: 1401021, Hilgenberg, Malsfeld, Germany) on the horizontal puller to yield a small and confined electric field around the tip. The current was controlled with an Iso-Stim 01DPI (NPI Electronic Insturments, Tamm, Germany) stimulator.

Following abortion criteria were defined: a) the onset of the postsynaptic current needed to be clearly separated from the stimulus artifact. b) The postsynaptic response must not scale with the stimulus intensity, but be all-or-none. c) The current needed to be monosynaptically. This was determined as no further increase in EPSC amplitude upon an increase of stimulation intensity or by inspection for a second (slightly) delayed component. Both events are assumed to result from stimulation of two distinct synapses within the electric field of the stimulation electrode. d) The holding potential needed to be stable throughout the recording. This conservative approach limited the number of analyzed synapses. 20 out of 31 synapses were excluded during analysis, some more directly due to online inspection during the experiment.

All recordings were Bessel-filtered at 2.9 and 10 kHz and digitized at sampling rates of 20 kHz. The recordings were measured in whole-cell mode at -70 mV and in current clamp at 0 pA unless noted otherwise. The Liquid Junction Potential (13.4 mV, calculated based on Barry and Lynch (1991)) was corrected for.

2.6.3 Post-Recording Imaging

In most cases a high resolution z-stack (153.45 x 153.45 μm^2 in 1024 x 1024 pixels and 1 μm z-steps) was taken post recording on the Leica SP5. To estimate the volume of the synapse a stack of images (minimum of 512 x 512 pixels) was taken at a higher magnification.

2.7 Immunohistochemistry

2.7.1 Fixed-Tissue Preparation

Mice were deeply anesthetized with isoflurane and transcardially perfused after a minimum of 14 days long post-injection period. Anesthetized mice were taped down on their backs, while maintaining the anesthesia with drops of isoflurane in a 15 mL falcon tube put over the nose. Before opening the abdomen, loss of reflexes confirmed the anesthesia. After the opening of the abdomen the diaphragm was loosened from the chest, the thorax widely opened, and the heart was freed of surrounding fatty tissue. A 0.6 mm steel needle was inserted into the left ventricle. An incision at the right ventricle released excess liquids. The blood circuit was flushed with 15 - 20 mL cold PBS followed by 15 - 20 mL 4 % PFA dissolved in PBS. Following the perfusion, the brain was removed from the skull and stored in 4 % PFA at 4 °C for post-fixation. Afterwards brains were stored in PBS at 4 °C until slicing. Slicing was done on a vibratome (Sigmann Elektronik, Hüffenhardt, Germany). Slice thickness ranged from 50 μm to 300 μm.

2.7.2 Immunohistochemistry

2.7.2.1 Antibodies

Table 2.3: **Primary Antibodies**.

antigen	host species	clone	source (Cat. No.)	dilution
VGLUT-1[a]	guinea pig	polyclonal	Millipore (AB5905)	1:1000
VGAT[b]	guinea pig	polyclonal	Synaptic Systems (131004)	1:250

[a]= vesicular glutamate transporter 1, [b]= vesicular GABA transporter

Table 2.4: **Secondary Antibodies.**

against	host species	fluorophore	source (Cat. No.)	dilution
guinea pig	rabbit	Alexa 594	Invitrogen (A-11076)	1:1000

2.7.2.2 Protocal

All steps are performed at room temperature and under gentle agitation, unless noted otherwise.

Slices were permeabilized and unspecific binding sites were blocked for 30 - 45 min in blocking buffer (VGLUT-1: 5 % NGS, 1 % BSA, 0.5 % Triton X-100 in PBS; VGAT: 5 % NGS, 1 % BSA, 0.3 % Triton X-100, 0.1 % cold fish skin gelantin in PBS). Then they were washed in vehicle solution (VGLUT-1: 2.5 % NGS, 0.2 % BSA, 0.5 % Triton X-100 in PBS; VGAT: 5 % NGS, 1 % BSA, 0.3 % Triton X-100, in PBS) for 10 min. The 1st antibody, diluted in the vehicle solution, was applied overnight at 4 °C. The next day, the tissue was washed 3 times in vehicle for 10 min each. The secondary antibody, also diluted in vehicle solution, was applied for 90 - 120 min under light protection. The tissue was finally washed twice in vehicle solution and twice in PBS for 10 min each. The slices were then mounted on coverslips covered in SlowFade (life technologies, Carlsbad, CA, USA).

2.7.2.3 Confocal Imaging

Confocal images were acquired on the Leica TCS SP5 microscope with the APO 63x objective. The scannerhead was set to 400 Hz line scanning rate and a resolution of 1024 x 1024 pixels. The field of view was usually 234.32 x 234.32 μm^2. The pinhole was adjusted to yield a z-resolution of 0.988 μm and focal planes were 1 μm spaced apart. Photomultiplier tubes enhanced the photon counts at a voltage of 900 V and the read-out was digitized with 12-bit resolution. In order to decrease the noise, frames were averaged 3 times during acquisition. GFP was excited with the 488 nm argon laser line and imaged in the range of 498 - 530 nm. The Alexa 594 fluorophore was excited excited with the 633 nm helium-neon laser line and imaged in the range of 645 - 675 nm.

2.8 Electron Microscopy

2.8.1 Photoconversion of DAB for Electron Microscopy

The principle of photoconversion is to transform 3,3'-Diaminobenzidine (DAB) into a local electron-dense precipitate. First, DAB monomers get crosslinked by radicles to form polymers. This so called precipitate has a high affinity for osmium, which appears as a dark

staining in electron microscopy (EM) images. This technique was first described by Maranto (1982).

The chemical reaction from DAB to a precipitate requires an oxidation step. Fluorescent excitation produces oxygen radicles, in the presence of ambient oxygen. The oxygen radicle can be harnessed to oxidize DAB. Due to the high reactivity, the oxygen does not diffuse far from the fluorophore and oxidizes DAB. The polymerized DAB is not able to diffuse, but reports the site of the fluorophore precisely.

In order to photoconvert DAB and screen for the identity of synaptic profiles an animal was injected with a SyPhy-2-pHluorin virus. The animal was sacrificed 14 days later and 200 μm slices were prepared (compare section 2.7.1). To increase the oxygen level of the medium, slices were incubated in 50 mL Tris-HCl, pH 7.6 for 120 min at 4 °C under constant oxygenation via a frit device (air stone). Following the 120 min the container was sealed and stored at 4 °C overnight to allow the oxygen to equilibrate in the tissue. Slices were then transferred to ice-cold, oxygenated 50 mL Tris-HCl buffer supplemented with 1 mg/mL DAB and 5 drops ($\approx$ 150 μL) of 1 M NaOH to adjust the pH to 7.2. From there the slices were transferred with the incubation medium to a custom-made chamber, which allows keeping the slices at a constant temperature of 4 °C, during the illumination under the microscope. The slices were flattened and immobilized by a nylon net, glued to a platinum ring, on the cover slip (Menzel-Gläser, grade 00, thickness 95 μm). The temperature was kept at 4 °C by pumping ice-cold water through the chamber's cooling unit. Under an inverse lightmicroscope (Leica DM IRBE), equipped with a 40x oil immersion objective (NA: 0.75 - 1.25), the GFP derivative was excited with a 100 W mercury discharge lamp at a wave length of 488 nm. The objective has a working distance of 175 μm. Under these conditions photons theoretically have a maximal penetration depth of 80 μm. The excitation lasted in total 11 to 12 min until all fluorophores were bleached. The NA of the objective was initially set to 0.75, changed to 1.0 after 4 min and finally to 1.25 after another 4 min.

Subsequent the slices were washed once in 50 mM Tris-HCl, pH 7.6 followed by three wash steps in 100 mM cacodylic buffer, pH 7.4. The region of interest was excised with a scalpel from the surrounding tissue. The sections were washed again in 100 mM cacodylic buffer for 1 h. They were post-fixated by 1.5 % potassium ferrocyanide/ 2 % osmiumtetraoxide in distilled water (dH$_2$O) for 60 min. The fixation solution was washed off by dH$_2$0 for 1 - 2 h in 3 steps. The sections were dehydrated by an ascending alcohol series followed by propylene oxide. It was finally stored in a 1:1 mixture of propylene oxide and epoxy resin overnight. The next day the sample was transferred into pure epoxy resin, horizontally oriented, and polymerized at 60 °C for 36 h. All chemicals used were purchased from SERVA (Heidelberg, Germany).

For EM the tissue block was serial sectioned with 38 nm thickness on an Ultracut S ultramicrotompe (Leica, Germany) equipped with a diamond knife angled at 35° (Diatome, Biel, Germany). The sections were collected onto hydrophilized silicon wafer strips and post stained with Reynolds lead citrate.

2.8.2 The Electron Microscope

The serial sections were imaged on a Zeiss 1530 (Zeiss, Germany) scanning electron microscope. The InLens detector at a working distance of 2.1 mm together with 3 keV acceleration voltage was used. A total area of 11.6 x 8.7 nm at a 10000x magnification with a resolution of 3072 x 2304 pixel was imaged.

2.9 Data Analysis

2.9.1 Electrophysiology

The analysis was done using Igor Pro (v6.2, WaveMetrics Inc., Lake Oswego, OR, USA) with custom written routines. Values are reported as mean ± standard deviation (SD), unless noted otherwise. All groups were tested for normality with the Shapiro-Wilk normality test. As one group was not normal-distributed, all tests were done with a non-parametric Mann-Whitney U-Test / Wilcoxon rank sum test.

2.9.2 Cell Morphology and Synaptic Distribution

2.9.2.1 Dendritic Length Between Stimulated Synapse and Soma

All images were processed with Fiji (Schindelin et al., 2012) and the Simple Neurite Tracer plug-in (Longair et al., 2011).

The Simple Neurite Tracer was used to measure the dendritic length between the soma and the synapse. The plug-in searches for the brightest trace of voxels in 3D between two or more manually selected spots. The output is the length of the trace.

2.9.2.2 Synaptic Volume of Stimulated Synapses

All images were processed with Fiji and additional plug-ins: FindFoci (Herbert et al., 2014) and 3D ROI Manager (Ollion et al., 2013).

The FindFoci plug-in was used to find the volume of the synapse. The search parameters were set to auto threshold (mean + 3x SD). Above the threshold local maxima were found. Starting from the local maxima all voxels above threshold were included into the volume. To insure that minor fluctuations in the signal intensity are not scored as individual volumes, the image was first filtered with Gaussian blur with 1 px range. Finally volumes were merged, if the saddle point between two local maxima was higher than 50 % of the peak height (peak intensity - threshold) of either peak. Volumes were excluded, if it contained less than 5 voxels. The segmented image was loaded into the 3D ROI Manger, with which the volume of the synapse of interest was calculated.

2.9.2.3 Synaptic Distribution Along the Radial Distance to the Soma

The image stacks, taken after patch-clamp recordings, and thus from alexa dye filled individual neurons, were analyzed in Fiji. In case the stimulation or the patch electrode were imaged, they were manually removed from the image. So were excessive noncytosolic alexa dye signals, which inevitably accumulate in the tissue during approaching the cell with the

patch-electrode. In order to reduce noise, the image was filtered with a 3D median filter (1 px radius). The image stack was adjusted for depth dependent intensity decay. The dendritic tree and soma was reconstructed with a manually selected threshold after the stack was processed with a "Statistical Region Merging" filter. For technical reasons (see below) the volume of the neuron had to be widened by 1 pixel along each axis.

The GFP signal was first filtered with a 3D median filter (1px radius). In order to reduce the background and possible inhomogeneities, the stack was 3D gaussian blured with a 6 µm isotropic radius and subtracted from the original image. The threshold was calculated as follows: for each image stack the images were subject to auto threshold with the IsoData filter. This filter thresholds the image such that the threshold equals or is larger than the middle between the mean of background and foreground. Next, the mean intensity and SD of all background voxels in the stack was calculated. The final threshold was set to the mean + 3x SD. Once thresholded, local maxima were found and the volumes filled to a level of threshold + 0.1x peak heights (maximum intensity - threshold). Volumes were excluded or merged to the neighboring volume, if it contained only one voxel. Volumes were also merged if the saddle point between two maxima was not lower than 75 % of the smaller peak intensity (saddle point < peak intensity - (peak intensity - threshold) x 0.25). In a subsequent processing step the segments were filtered again to have a minimal mean intensity of mean background + 5x SD.

Once the binary images of the neuron and the GFP positive synapses were available the 3D ROI Manager was used to calculate the overlap of synapses with the neuron. Touching synapses had an overlap with the neuron, as it was widened by 1 pixel and could thus be filtered out from non-touching synapses. Additionally the center of mass per synapse and the neuron was calculated. The length of the vector between the centers of masses was taken as the distance to soma. Additionally the volumes of the synapses were calculated.

2.9.3 Immunohistochemistry

2.9.3.1 Synaptic Volume

Similar to the synaptic volume of stimulated synapses in electrophysiology the FindFoci plug-in was used. First images were filtered with a 3D median filter (2 px radius) to reduce noise. The following procedures were as described in 2.9.2.3 for the GFP signal.

2.9.3.2 Immunohistological Signal Detection

The thresholding procedure was the same as for the synaptic GFP signal (2.9.2.3). Noise was reduced by a 3D median filter. The background, i.e. a Gaussian blured image, was subtracted. The images were initially thresholded with the IsoData filter and then the mean and standard deviation of the background was calculated. The threshold (mean + 3x SD) to binarize the images was again averaged across all stacks taken from the same preparation and same day. As the signal of the antibody staining was strongly correlated with the depth into the tissue, the threshold was adjusted by the following factor: mean intensity of the focal plane divided by the mean intensity of the stack.

2.9.3.3   Co-Occurrence

The segmented synaptic-GFP stack was loaded into the 3D ROI Manager. The volume, the mean intensity, and the overlap with the binarized immunohistlogical image stack were calculated. As a control for overlap by chance the images were rotated against each other by 90° steps and the overlap was calculated for each rotation (90°, 180°, 270°).

2.9.4   3D Reconstruction of Ultrastructure

The EM images were loaded as a stack in OpenCar (http://opencar.ulster.ac.uk). The sections were manually aligned using features that persisted across multiple sections. The following ultrastructural features were outlined in each of the consecutive sections: presynaptic terminal, postsynaptic dendrite, vesicles, mitochondria in the terminal, glia (ensheathing the terminal and dendrite), and postsynaptic densities (PSD), whenever visible. With the outlines and information about the thickness of the slice OpenCar rendered 3D objects. The objects were transferred to and visualized in Amira (Visage Imaging, Richmond, Australia).

2.10 Contributions

Virus productions were carried out by Claudia Kocksch. The tissue preparation for EM and the image acquisition were done by Heinz Horstmann. The image analysis for the distribution of synapses along the dendrites was supported by Dr. Hongwei Zheng. And finally some routine slicing of fixed tissue was handled by Marion Schmitt.

3 Results

3.1 Basic Electrophysiological Characterization of MD Relay Neurons

The major focus of the thesis was on the electrophysiological characterization of mediodorsal thalamic neurons and the synaptic contacts formed by axons from the piriform cortex. Therefore, I first investigated some passive and active properties of the MD neurons.

MD neurons have a resting membrane potential (V_{rest}) of -75.8 ± 7.1 mV (n = 64) (Figure 3.1 A). The membrane potential (V_m) change during a 500 ms/-100 pA current injection yields a membrane resistance (R_{mem}) of 192.1 ± 68.9 MΩ, according to Ohm's law (Figure 3.1 C). Additionally, I looked at the characteristics of the action potentials (AP). A ramp current injection depolarized the neurons to the action potential threshold. The action potential threshold is defined as the potential at which the slope of the depolarization increases abruptly for the first time due to the sodium-channel opening, as compared to the sole current injection. MD neurons have an action potential threshold of -50.7 ± 4.8 mV (Figure 3.1 A). Furthermore, I evaluated the AP-afterhyperpolarization (AHP), here defined as the peak of action potential repolarization relative to the threshold. The MD neurons have an AHP of -14.2 ± 2.8 mV (Figure 3.1 B). The neurons, in which unitary EPSCs could be evoked by juxtasynaptic stimulation of a labeled synapses (represented by filled circles), had a significantly lower R_{mem} (118.6 ± 45.4 MΩ vs. 199.2 ± 66.7 MΩ; W = 553, p = 0.002) than the other neurons. They did not differ in any of the other parameters examined (V_{rest}: W = 257, p = 0.296; V_{thres}: W = 298, p = 0.916; AHP: W = 337, p = 0.488).
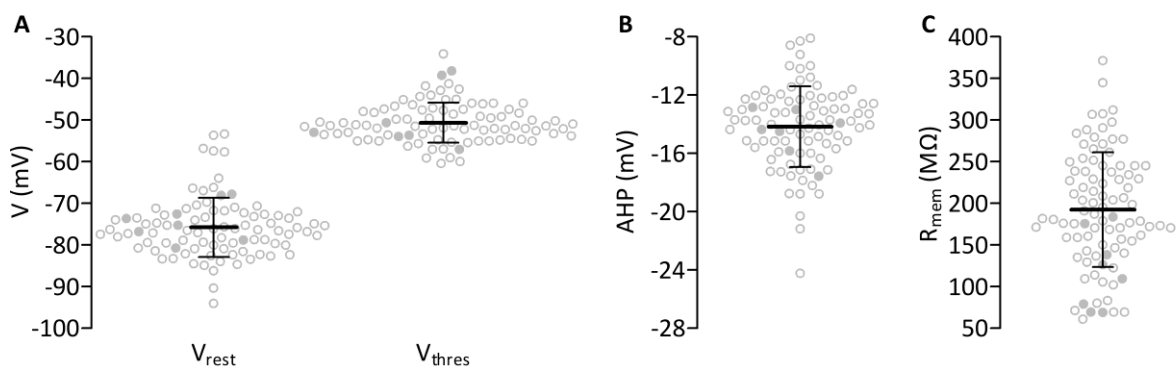

Figure 3.1: **Basic Characterization of MD Neurons**. (**A**) membrane resting potential (V_{rest}) and action potential threshold (V_{thres}). (**B**) Afterhyperpolarization (AHP). (**C**) Access membrane resistance (R_{mem}). Filled circles represent neurons, which responded with a unitary EPSC upon stimulation of labeled synapses (n = 8), open circles represent neurons used for T-type calcium channel current analysis (n = 56).

3.1.1 Low-Threshold Activated Calcium-Currents

A prerequisite for the differential firing modes - tonic and burst - are the T-type calcium-currents (I_T). They are conducted via low-threshold activated calcium-channels, also known as T-Type channels. When a neuron is hyperpolarized, a small depolarization may trigger a Ca^{2+}-influx, which in turn depolarizes the neuron above threshold and therefore elicits a train of action potentials - the AP-burst. If the neuron is more depolarized at rest, the channels are inactivated and do not support the firing of bursts. To allow burst firing, the T-type channels need to be recovered from inactivation via hyperpolarization.

In order to measure the kinetics of the recovery from inactivation, I first inactivated the channels with a depolarization step and then tested the relative amplitude of the current with a second depolarizing stimulus at variable interstimulus intervals. The interstimulus intervals had a duration of 200 ms with 200 ms increment. I elicited I_T via a 1 s depolarization step from the holding potential of -100 mV to -60 mV (Figure 3.2 A). An exponential fit of the average ratio of the peak amplitudes against the interstimulus interval yields a time constant for the recovery from inactivation of 0.41 ± 0.02 s (Figure 3.2 C). The mean current amplitude is 2915 ± 1664 pA (n = 56).

The recovery from inactivation of the Ca^{2+}-channels also depends on the membrane potential. When MD neurons are hyperpolarized by current injections (Figure 3.3 A1), the latency of the first action potential riding on the calcium-mediated low-threshold spike (LTS) subsequent to the end of the current injection becomes shorter the more hyperpolarized the neuron has been (Figure 3.3 A2).

Both, the time and membrane potential dependency of the channel, interplay to shape the response of the neurons to brief hyperpolarization. To test the latency of the first action potential after a variably long hyperpolarization pulse, I injected -300 pA for 50 ms prolonged in 50 ms increments (Figure 3.3 B1). The longer the hyperpolarization persists, the shorter is the latency for the first action potential riding on the LTS after the end of the current pulse (Figure 3.3 B2).
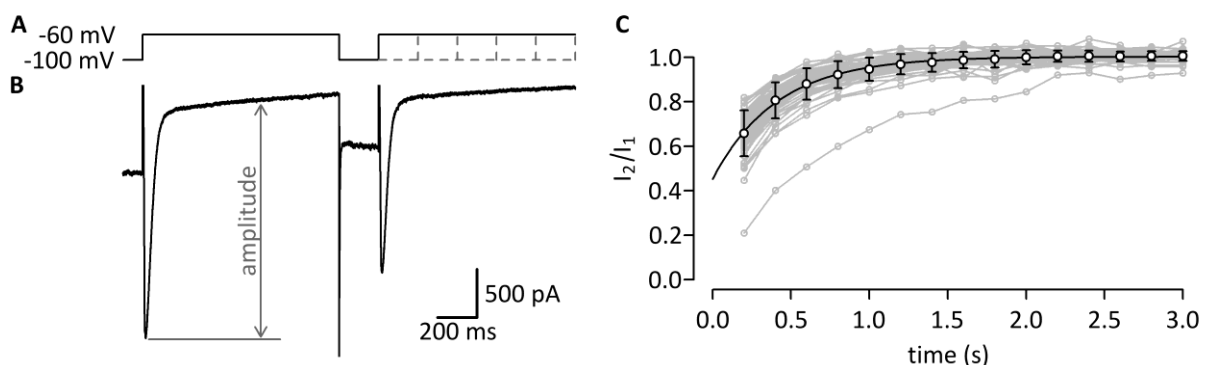

Figure 3.2: **Recovery of I_T.** (**A**) The stimulus protocol depolarized the neuron from holding potential (-100 mV) to -60 mV for 1 s and after an interstimulus interval of 200 ms plus 200 ms increments depolarized a second time (1 s). (**B**) Example showing a typical current trace in response to the stimulation shown in (A). The amplitude is measured from peak to base line of a double exponential fit. The double pointed arrow spans an approximation of the amplitude. (**C**) The ratio of the current amplitudes of the second (I_2) to first (I_1) depolarization step is plotted against the interstimulus interval for all neurons (gray, n = 56) and their average (open circles). The average data is fitted with an exponential curve (0.41 ± 0.02 s) (black line).

In summary, I determined some passive and active properties of the MD neurons. V_{rest}, R_{mem}, AHP, and V_{thres} are is the normal range of thalamic relay neurons. MD neurons express high enough levels of low-threshold activated calcium-channels to help shape the input-output function of MD neurons.
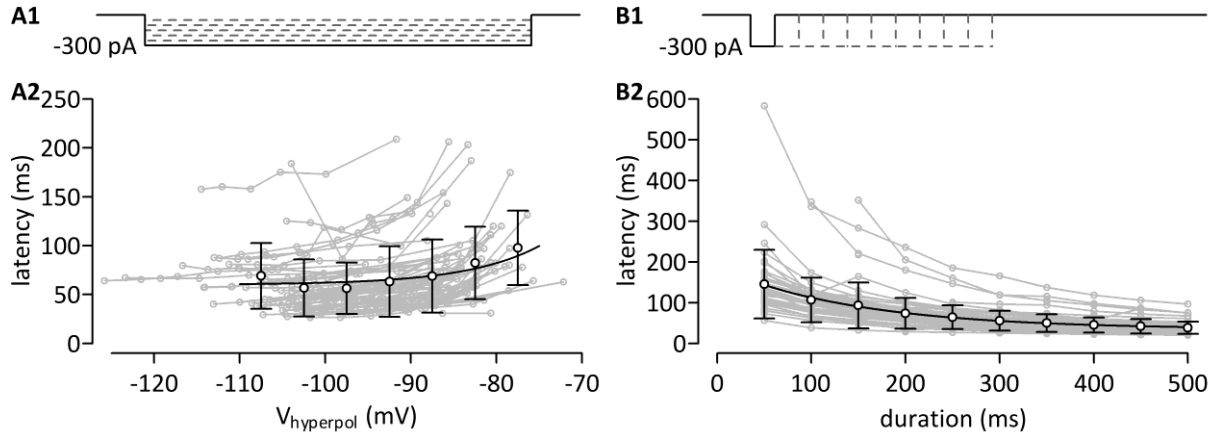

Figure 3.3: **I_T Evokes Action Potentials**. (**A1**) Current step protocol from -300 pA to -50 pA (relative to the holding potential) in 50 pA increments with a pulse width of 500 ms. (**A2**) The latency of the first action potential's peak after the release of the current injection depends on the potential during the hyperpolarization ($V_{hyperpol}$). Individual neurons are displayed as connected circles in gray. The averages, in 5 mV bins, is represented by the open circles and they are fitted by an exponential function (black line). (**B1**) Current step protocol to -300 pA for 50 ms prolonged in 50 ms increments. (**B2**) The latency depends on the duration of the hyperpolarization. Symbols are as in (A2).

3.2 Distribution of PIR Synapses on MD Neurons

Alongside the electrophysiological characterization of the PIR-MD synapse, also its distribution and ultrastructure is of interest. Therefore, I first looked at the distribution of PIR synapses long the radial distance from the soma. I prepared acute brain slices from mice that received AAV injections in the PIR, which subsequently expressed the synaptophysin-GFP fusion protein and thus a synaptic marker. After filling the neuron with alexa dye, I acquired high resolution confocal microscopy stacks of the neurons. The imaged synapses were evaluated for their distance to the somatic center of mass (Figure 3.4 A) and their average size in different distance ranges (Figure 3.4 B).

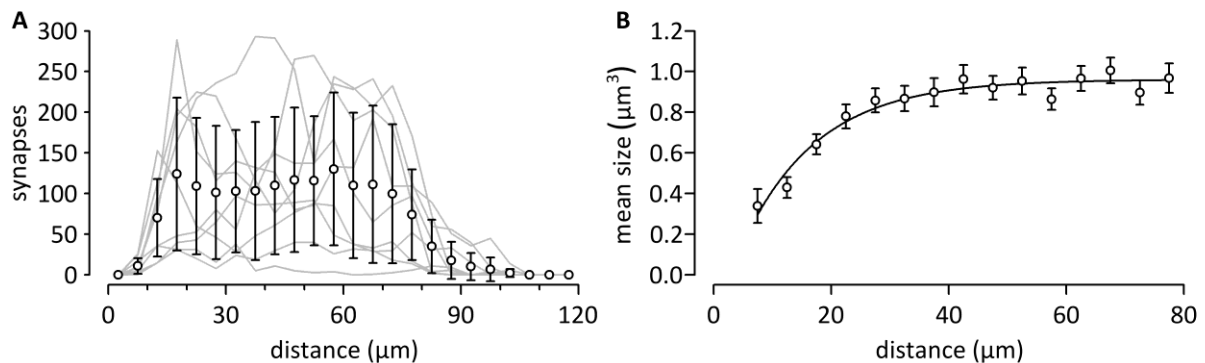Figure 3.4: **Synaptic Distribution.** (**A**) The average number of synapses relative to the distance to the somatic center of mass in 5 µm bins. The underlying raw data of the 9 neurons is shown in gray. (**B**) The mean size (± SEM) of synapses in the range of 5 to 80 µm in 5 µm bins. Outliers (> 25 µm) were excluded. An exponential fit describes the size to distance relationship (black line).

The number of synapses touching the dendrites initially increases and reaches a plateau level at ~15 µm away from the soma (Figure 3.4 A). The low number of synapses within the first 15 µm is due to the fact that the respective volume around the center of mass is usually part of the soma and can therefore not contain synapses. At around 70 µm the number of synapses starts to decrease again, as the dendritic tree thins out. In 4 out of 9 cases the distribution shows an initial peak of the number of synapses within 30 µm. For the remaining 5 analyzed neurons the number of synapses increases steadily with the radial distance (until ~70 µm) or they have a homogenous distribution independent of the distance. I further analyzed the synapses, grouped by their distance from soma in 5 µm bins, in respect of their size (Figure 3.4 B). Synapses proximal to the soma are on average smaller than synapses more distally. The size increases as an exponential decay function of the distance.

3.3 Ultrastructure of PIR-MD Synapses

Another morphological aspect of the differentiation between thalamic driver and modulatory synapses is the ultrastructure of the synapses. Drivers are described as larger and harboring multiple mitochondria and active zones. In order to investigate the ultrastructure, AAVs were used to allow for pHluorin-tagged synaptophysin expression in PIR neurons. The injection site covered the full PIR and some minor spill over to the agranular insular cortex and somatosensory cortex. After reaching steady state expression levels at 21 days post injection, the tissue was prepared for electron microscopy. In short: the high probability to form oxygen radicals by the pHluorin protein was utilized to form electron-dense DAB precipitate within the axons and thereby label structures originating from PIR. Labeled structures therefore appear darker than the unlabeled surroundings in electron micrographs.

Serial sectioning of the tissue allows tracing structures across multiple sections and extraction of their 3-dimensional morphology (Figure 3.5 & 3.6). This supplies more information than a single randomly placed crosssection. Within the inspected tissue block three RL-type terminals, i.e. morphologically driver synapses, were fully reconstructable (Figure 3.6 A & B). Two more giants were partially included in the examined volume (Figure 3.6 C). The largest complete synapse takes up a volume of 2.27 μm^3, the remaining two 1.34 and 0.75 μm^3. The diameter goes up to 3.5 µm. They all contain multiple mitochondrial profiles across most sections. The 3D reconstruction confirmed that these truly are separate mitochondria. These synapses contain 8, 5, and 5 mitochondria respectively, which take up 19.93, 20.35, and 24.12 % of the total volume. The two incomplete reconstructions contain 8 and 13 most likely separate mitochondria. In some synapses small multivesicular bodies are apparent (Figure 3.5 A). All synapses are well darkened by DAB-precipitate around the dense accumulation of vesicles. Individual vesicles often do not stand out enough to be labeled, although the overall appearance clearly indicates their presence. In the cross-sections often multiple dendritic "islands" appear within the labeled presynaptic profile (Figure 3.5). These are part of a dendritic outgrowth, also known as excrescences. The number of excrescences is not limited to one, but multiple outgrowths may penetrate the PIR-MD synapse. The
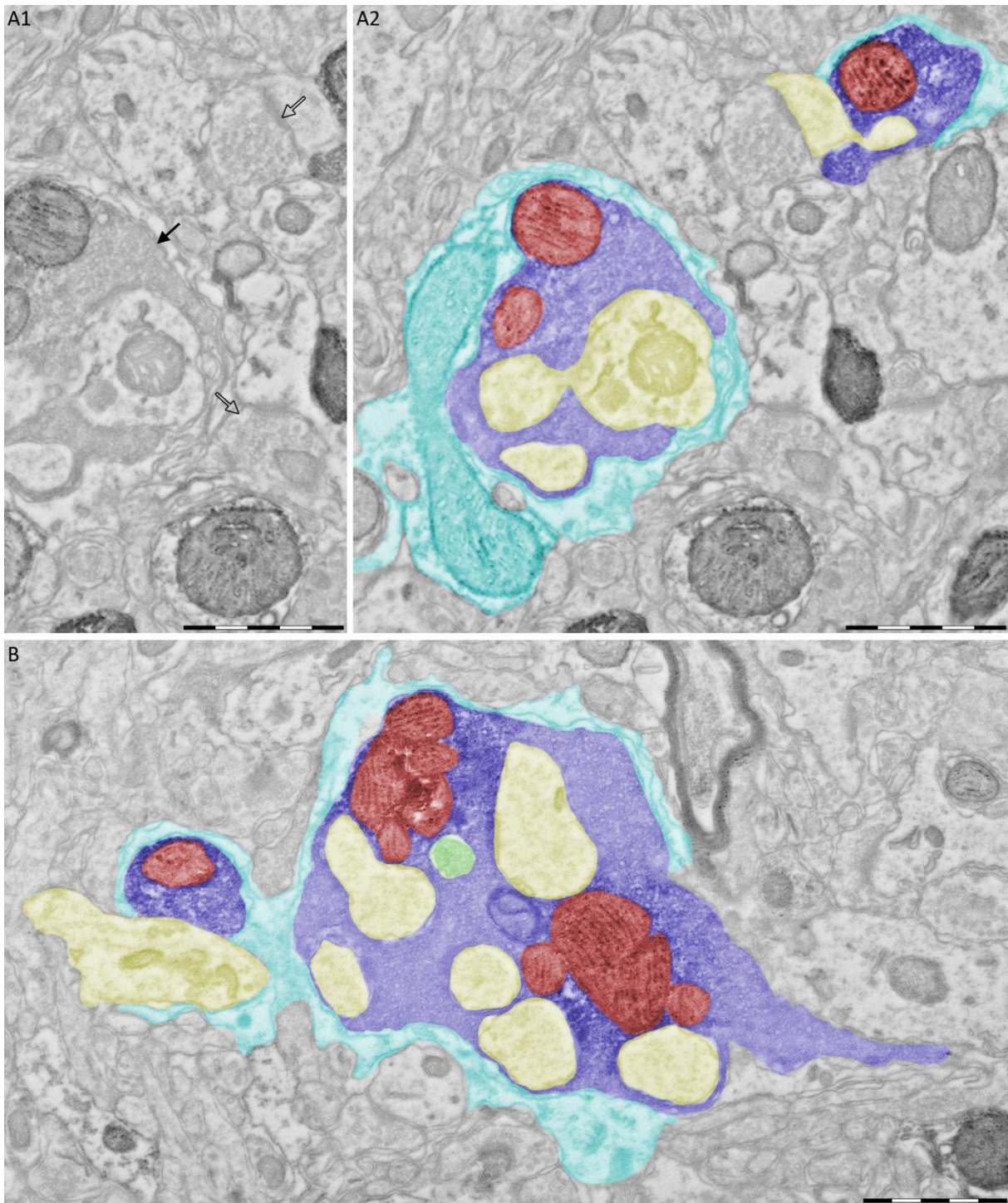
Figure 3.5: **PIR-MD Synapse Cross-Sections.** (**A1**) Electron microscopic cross-section through a labeled RL-type synapse in the MD. The solid arrow points towards the labeled RL-synapse, the two open arrows point towards unlabeled smaller synapses. Labeled and non-labeled synapses are separated by their darker and lighter background respectively. (**A2**) Two highlighted RL-type boutons in the same cross-section as in (A1). In this particular section is in the larger two, in the smaller one mitochondria apparent. In both cases the dendrite has excrescences invading into the bouton, which are fully engulfed. The "island" of dendrite is connected to the larger part in adjacent cross-sections. Both boutons are covered by a glial sheet. (**B**) Two more examples of RL-type profiles. Both boutons have multiple mitochondria, although only one is apparent in the smaller bouton in this particular cross-section. The dendrite is also connected to the larger profile in adjacent sections. The larger bouton shows multiple "islands" of dendrite and one multivesicular body is apparent. In both cases the bouton is filled with vesicles. Both boutons are sheeted by the same glia lamellae. Blue = presynaptic terminal, yellow = post-synaptic dendrite, red = mitochondria, green = multivesicular body, cyan = glial sheet. Scale bar = 1 µm. EM-images were kindly provided by Heinz Horstmann.

presynaptic profile usually engulfs the postsynaptic dendrite partially and these spine-like excrescences of the dendrite fully (Figure 3.6). In this tissue preparation it is impossible to undoubtedly identify docked vesicles and the dendritic postsynaptic density (PSD), as well as *puncta ad-haerentia*. The correct number of active zones can therefore not be accurately determined. Regularly, but not always, a clear glial lamella encloses the presynaptic profile and on rarer occasions the dendrite (Figure 3.5). This constellation is called a glomerulus. In one case the presynaptic profile borders on a soma over a stretch longer than 1 µm in multiple consecutive slices. However, since no PSD is apparent in the soma and the putative presynaptic terminal is also penetrated by a dendrite, which is most likely not connected to this particular soma, a functional connection between the two cannot be unambiguously determined. Within the examined volume is also evidence that two synapses contact the same dendrite less than 2 µm apart (Figure 3.5 A & 3.6 C). Yet, as both are at the edge of the inspected tissue block, their volume cannot be measured.
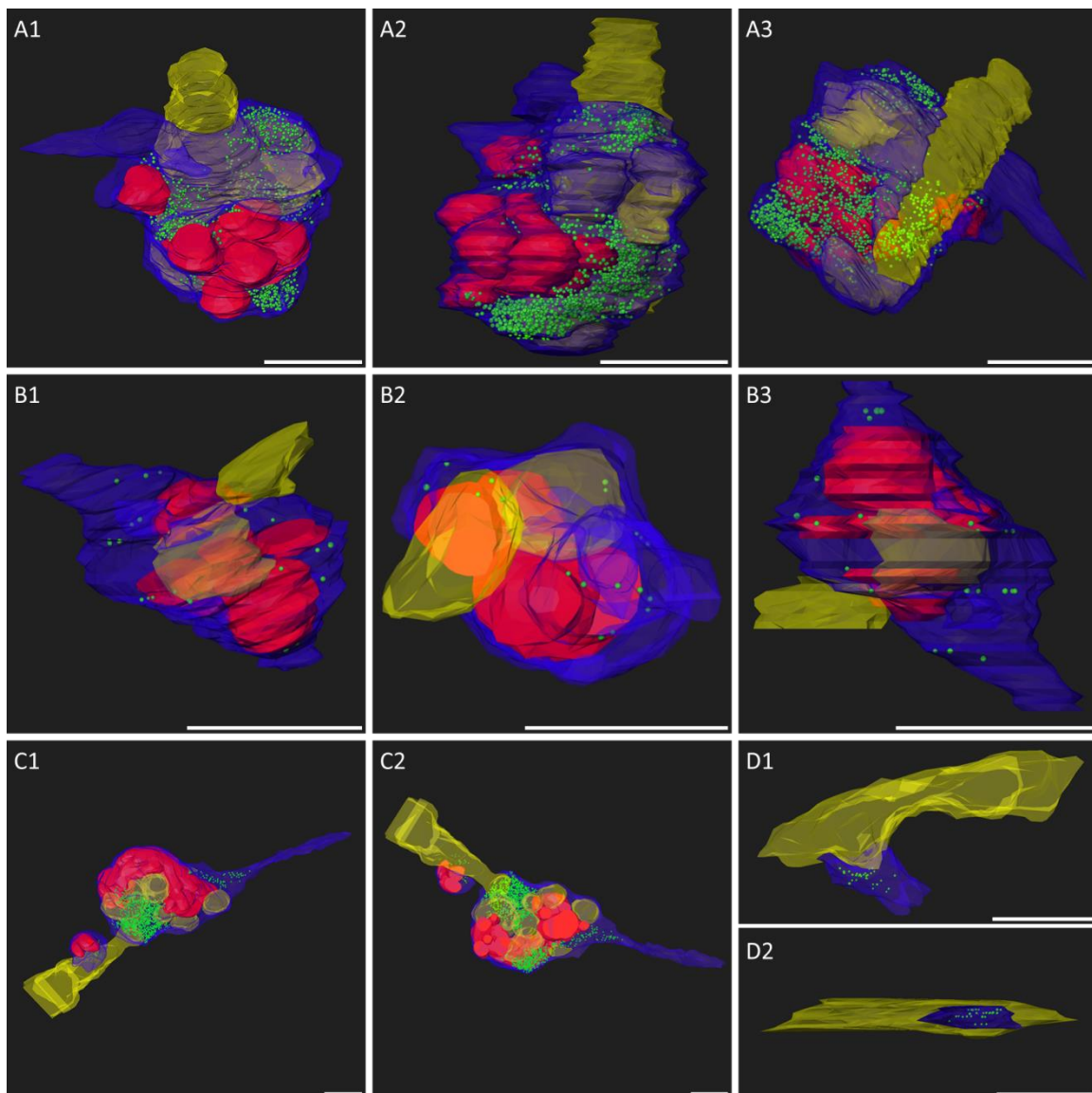
Figure 3.6: **3D Reconstruction of PIR-MD Synapses From Serial Sections.** (**A-C**) Reconstruction of RL-type synapses. The reconstruction in A corresponds to the larger synapse and B to the smaller one in Figure 3.5 A2; reconstruction in C corresponds to Figure 3.5 B. (**1-3**) different angles of the synapses. (**D**) A RS-type synapse without a mitochondrion. Blue = presynaptic terminal, yellow = post-synaptic dendrite, green = vesicles, red = mitochondria. Scale bar = 1 µm. Underlying EM-images were kindly provided by Heinz Horstmann.

In summary, the synapses are packed with mitochondria and vesicles with little to no "free" lumen. They wrap the dendrite partially and the spine-like excrescences fully and are themselves often covered by glial sheets.

I also reconstructed a RS-bouton (Figure 3.6 D). It contains no mitochondria and occupies only 0.048 µm^3. The vesicles the RS-bouton have a round shape as well.

On a different note: I observed 12 potential axo-axonal synapses, which contact the neurites of labeled neurons (Figure 3.7 A - E). The 4 neurites are identified as axons from PIR neurons by their darkened mitochondria. Some neurites contain membranous compartments. The presynaptic sides of the potential axo-axonal synapses are small (<1 µm). They contain up to 2 mitochondria and round vesicles. Only one PSD-like electron-dense structure per contact was detected. In one case there was a potential axo-axonal synapse between a labeled RL-type structure and a labeled neurite (Figure 3.7 F). The presynaptic side displays features indicative of a driver synapse, i.e. 4 mitochondria and a large diameter (~2 µm). Along the shared border of axon and synapse, multiple PSDs or PSD-like electron dense structures were apparent. The vesicles are also round.

In summary, giant RL-type PIR-MD synapses have multiple mitochondria, contain many round vesicles, and have a complexly shaped touching surface with the dendrite and its excrescences. Additionally, axo-axonal contacts of small synapses onto labeled axons and additionally one contact between labeled presynapse and labeled axon were detected.

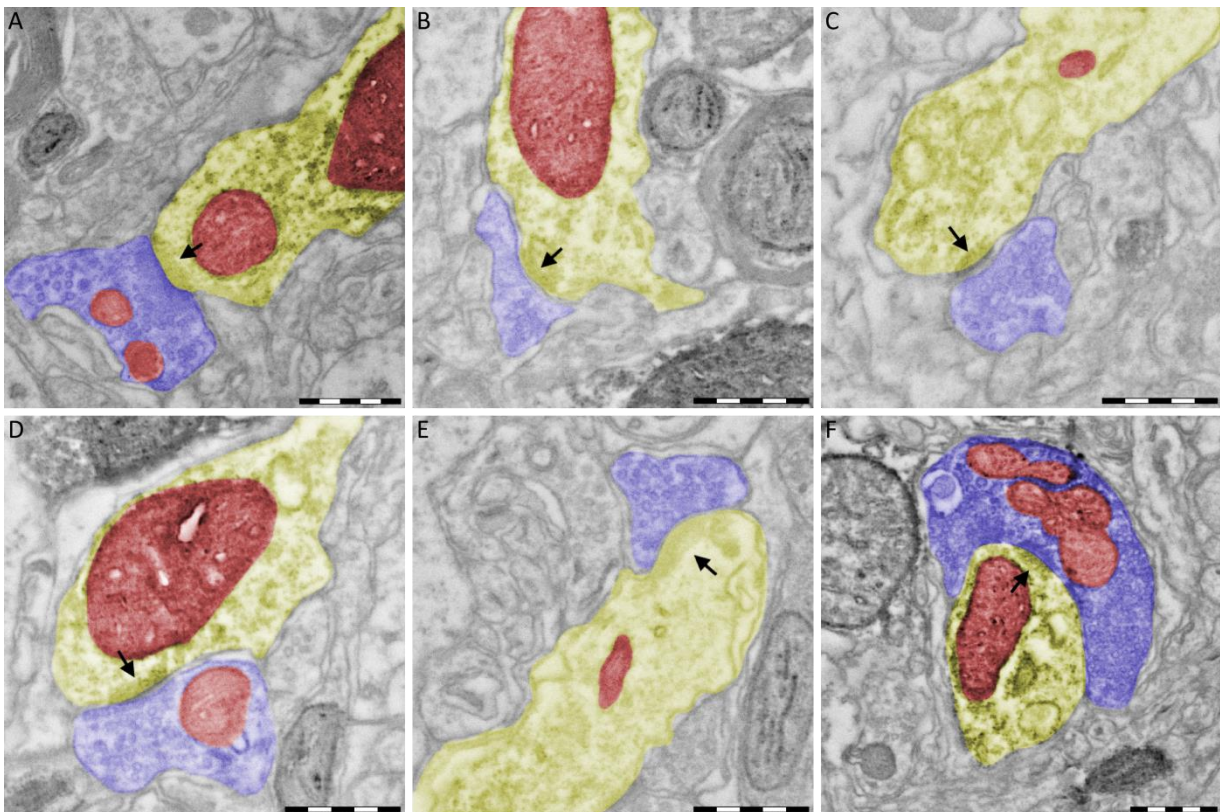Figure 3.7: **Axo-Axonal Synapses in the MD**. (**A-E**) Small terminals form synaptic contacts on labeled PIR-axonal profiles. (**F**) A large labeled presynaptic profile forms a synaptic contact on a labeled axon. Blue = presynaptic profile, yellow = postsynaptic profile, red = mitochondria. Arrows point to the postsynaptic density. Scale bar = 0.5 µm. EM-images were kindly provided by Heinz Horstmann.

3.4 Functional Properties of PIR Synapses

PIR-MD synapses are putative glutamatergic driver and modulatory synapses. My aim was to stimulate the driver-type synapses identified by their size. The stimulator passed bipolar square pulses of up to 90 V and 100 µs through the juxapositioned stimulation electrode. Upon successful and reliable stimulation, I tested the all-or-none principle, indicative of a monosynaptic contact and consistent with the fact that a presynaptic action potential triggered release (Seol and Kuner, 2015). Therefore, I stimulated the synapse with 10 stimuli at 20 Hz with increasing stimulation intensity (10 - 90 V). Furthermore, the contact had to meet the following criteria: clear separation of stimulation artifact and postsynaptic current and no sign of a slightly delayed second component. Post-hoc analysis included a stable holding potential throughout the recording as a factor. 20 out of 31 recordings did not meet all the requirements and were dismissed during analysis.

The basic characteristics of the EPSC evoked by the PIR-MD synapse are summarized in Figure 3.8. The EPSC amplitude is on average 391.2 ± 522.3 pA (n = 8). The current rises from 20 to 80 % in 0.54 ± 0.08 ms. After the peak, the current decays back to baseline with a time constant of 2.25 ± 0.97 ms. The stimulated synapses were on average 47.0 ± 15.8 µm away from the soma.

The EPSC amplitude does not depend on the size of the synapse in a linear manner (Figure 3.8 G). Moreover, the distance between synapse and soma is not correlated to the EPSC
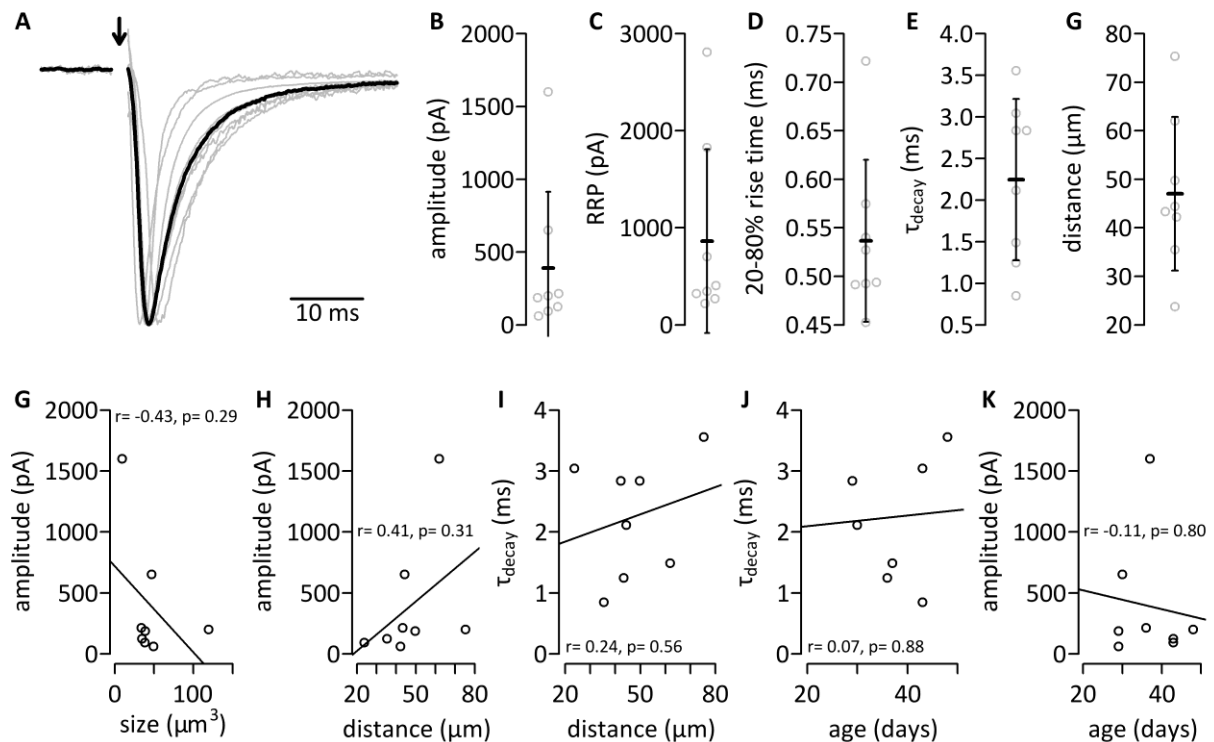
Figure 3.8: **PIR-MD Synapse Characteristics**. (**A**) All normalized EPSCs (gray lines) and their average (black). The stimulus artifact was removed (arrow). (**B**) Scatterplots of amplitude, (**C**) readily releasable pool, (**D**) rise time, (**E**) decay time constant, and (**F**) the distance between soma and synapse. (**G**) The amplitude does not correlate with the size of the synapse (Pearson correlation: r = -0.43, p = 0.29). (**H**) The amplitude does not correlate with the distance (r = 0.41, p = 0.31), (**I**) nor does the decay constant (r = 0.24, p = 0.56). (**J, K**) Both measures also do not correlate with the age of the animal (r = 0.07, p = 0.88; r = -0.11, p = 0.80).

amplitude (Figure 3.8 H) or the decay kinetics of the EPSC (Figure 3.8 I). The age of the mice within the span of 29 to 48 days does neither affect the amplitude (Figure 3.8 K), nor the decay kinetics (Figure 3.8 K).

Furthermore, I estimated the readily releasable pool (RRP) size. The RRP estimate is based on a method proposed by Schneggenburger et al. (1999). A train of 25 stimuli at 50 Hz depletes the RRP, such that ideally the later EPSCs solely depend on newly replenished synaptic vesicles. This stage is reached when the EPSC amplitude is in a depressed steady state. Assuming a constant replenishment rate from the first EPSC onward, the readily releasable pool can be extrapolated from the cumulative EPSC amplitudes by a linear regression of the linear part of the curve (Figure 3.9). The RRP for the PIR-MS synapse is 862.2 ± 947.5 pA. The release probability, i.e. the fraction of the RRP released by a single presynaptic AP, is on average 49.7 ± 21.6 %.

To examine short-term plasticity, I stimulated the synapse with trains of stimuli at different frequencies (1, 5, 10, 20, 50, 100 Hz). As expected the synapse exhibits short-term depression during repetitive stimulation (Figure 3.10 A). The steady state of the depression is frequency dependent. At 50 Hz the EPSC amplitude drops to 18.3 %. The synapse is able to follow 20 Hz quite reliably, while at 50 Hz the failure rate increases over time, i.e. with every consecutive stimulus (Figure 3.10 B). The failure rate rises up to a maximum of 47.5 % within the 1 s stimulus train. The synapses could not follow the 100 Hz stimulation. Similar to the steady state of the depression, the kinetics of the depression depends on the stimulus frequency (Figure 3.10 C).

The term "short-term plasticity" intrinsically implies that the depression persists only for a short duration. In order to analyze the recovery from depression, I depleted the vesicle pool of the synapse with a train of 25 stimuli at 50 Hz. To probe the recovery of the synapse, I applied a second identical train following increasing time intervals. The extent of recovery is calculated by the ratio of the amplitude of the first EPSC in the second train and the first amplitude of the depletion train. The synapse recovers with a time constant of 1.34 ± 0.29 s (Figure 3.11).
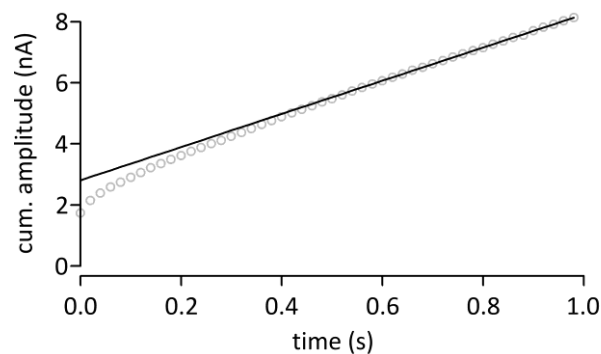

Figure 3.9: **Readily releasable pool (RRP)**. The cumulative amplitude of 25 consecutive stimuli in a 50 Hz train is plotted against time. A linear regression of the last 10 stimuli, i.e. within the linear part of the curve, is extrapolated. The intersection with the ordinate marks the RRP.
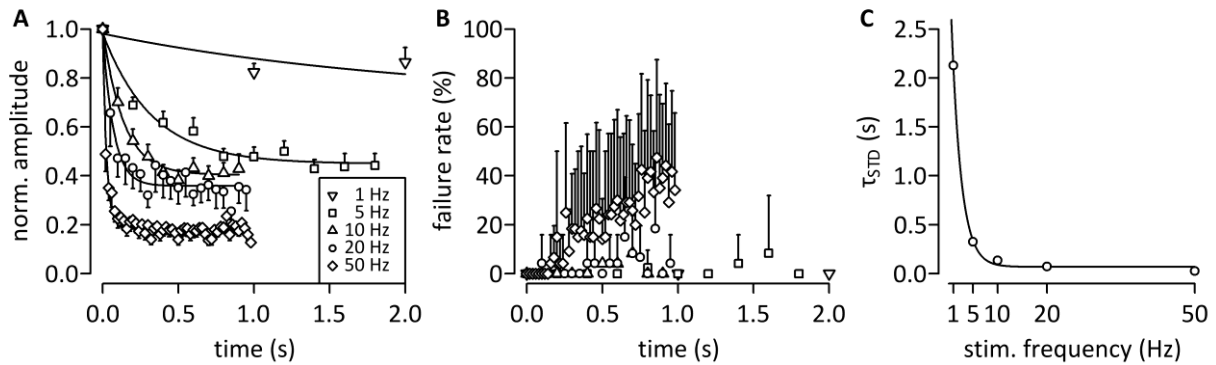
Figure 3.10: **Short-Term Depression (STD) of the PIR-MD Synapse**. (**A**) The normalized amplitudes of EPSCs during trains of stimuli at 1 to 50 Hz (mean ± SEM (unidirectional), n = 8). The depression is fit monoexponentially. (**B**) Failure rate of stimulation. Symbols as in (A). (mean ± SD (unidirectional), n = 8) (**C**) The time constants of the depression are plotted against the simulation frequency. The decay constants are themselves monoexponentially depended on the stimulation frequency.
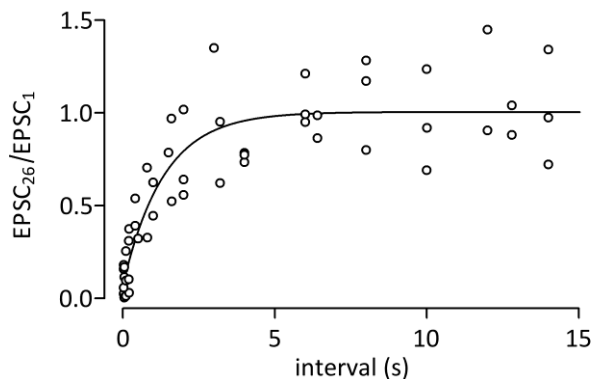

Figure 3.11: **Recovery From STD**. Synapses (n = 5) were first stimulated 25 times at 50 Hz to deplete the vesicle pool. Following a variable interval an identical test train was applied. The recovery rate is calculated as the amplitude of the first EPSC in the train ($EPSC_{26}$) normalized by the first EPSC in the depression train ($EPSC_1$). Outliers, i.e. $EPSC_{26}/EPSC_1 > 4$, were dismissed. The pooled data is fitted by a monoexponential function ($\tau = 1.34 \pm 0.29$ s).

3.5 Postsynaptic Actionpotential Triggering

When looking at the postsynaptic potentials in current clamp only 1 out of the 8 (= 12.5 %) synapses was able to evoked an action potential in the postsynaptic neuron upon electric synaptic stimulation (Figure 3.12). The percentage drops to 4 %, when considering all 25 neurons, for which the test protocol was started, but from which most had to be excluded from further analysis for various reasons. Dependent on the membrane potential just before the stimulus (V_{pre}) the neuron fired multiple action potentials (burst mode) or just a single one (tonic mode) (Figure 3.12 B). The amplification of the input comes at the cost of signaling speed. The first action potential during tonic mode fires at a shorter latency than during burst mode, as the burst mode requires I_T (Seol and Kuner, 2015) as an additional component of the signal transduction cascade to become effective (Figure 3.12 A & C).

In order to estimate the minimal required EPSC amplitude to trigger action potentials, I injected current trains of 3 artificial EPSCs (aEPSCs) at 1 Hz and 0 pA holding current. The individual aEPSCs were shaped to have the following characteristics: 20 - 80 % rise time: 0.80 ms and decay constant: 2.55 ms. Due to technical limitations the initial amplitude of
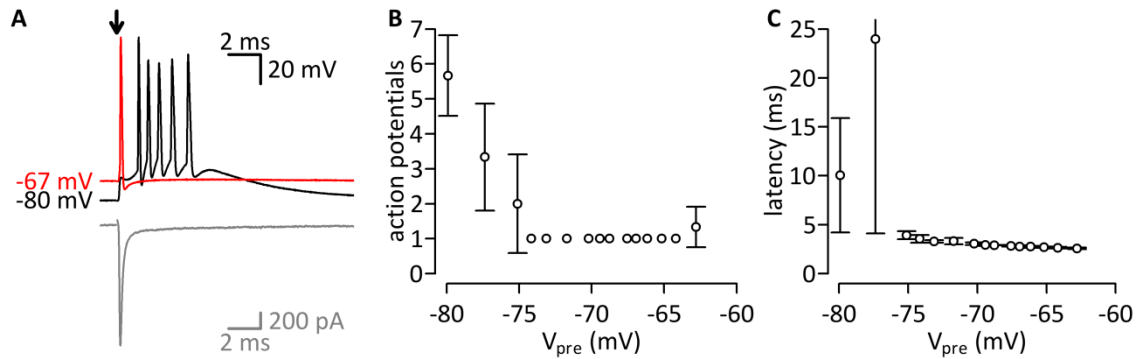
Figure 3.12: **The Driving PIR-MD Synapse**. (**A**) Time matched voltage (red, black) and current response (gray) of one PIR-MD synapse stimulation. The voltage response is shown for two different membrane potentials. The stimulation artifact was removed (arrow). (**B**) As typical for thalamic relay neurons this neuron switched from burst to tonic mode with increasing membrane potential (V_{pre}). At low V_{pre} this neuron fired multiple action potentials, while at more depolarized V_{pre} it faithfully transmitted a single action potential for each stimulus. (**C**) The latency until the peak of the first action potential decreases with increasing V_{pre}.

100 pA was raised in gross 100 pA increments to a maximum of 1000 pA. The amplitude was scored as sufficient, if the neurons responded to all aEPSCs with action potentials. Neurons, which required more than 1000 pA (8 out of 58 neurons), were assumed to have a threshold of 1100 pA. Finally, the minimal amplitude of an aEPSC to trigger postsynaptic action potentials from rest needs to be 758.6 ± 244.3 pA (n = 50 + 8). Therefore the average EPSC amplitude is only 51 % of the required stimulus. It drops to 19%, when excluding the two largest EPSC amplitudes, which are clearly separated from the remaining ones.

3.5.1 Could Some PIR-MD Synapses be GABAergic?

I also measured the reversal potential of the EPSCs or EPSPs in current clamp or in voltage clamp mode respectively (Figure 3.13). I stimulated the synapses at increasing holding current or membrane potential, respectively. The rationale is to find the potential at which there is no net current flow. 2 out of 11 synapses had a positive reversal potential, as expected for glutamatergic projections (Figure 3.13 B). The remaining synapses had a negative reversal potential (Figure 3.13 B). Considering the high chloride concentration of the intracellular patch electrode solution (20.7 mM), this is closer to a theoretical V_{rev} of a chloride driven current than a sodium one. Therefore the synapses could be GABAergic.

Before confirming the neurotransmitter profile of the putative GABAerigc synapses and identifying their origin, I analyzed if the "space-clamp" issue could introduce a systematic error, explaining the deviation from the expected sodium reversal potential. "In nonspherical cells, such as neurons, the membrane potential is not clamped distal to the voltage-clamp electrode" (Bar-Yehuda and Korngreen, 2008). The amount of deviation from the clamping voltage is proportional to the distance to the voltage-clamp electrode, the geometry of the neuron and active as well as passive conductance properties of the membrane. Here only the distance between soma and synapse is considered, as it is the major factor determining the electrotonic decay along dendrites (Figure 3.14 A). However, a simplistic model predicts a systematic error towards the estimate of a more depolarized reversal potential (Figure 3.14 B). This can therefore not explain the variation towards negative V_{rev}s. On top, V_{rev} does
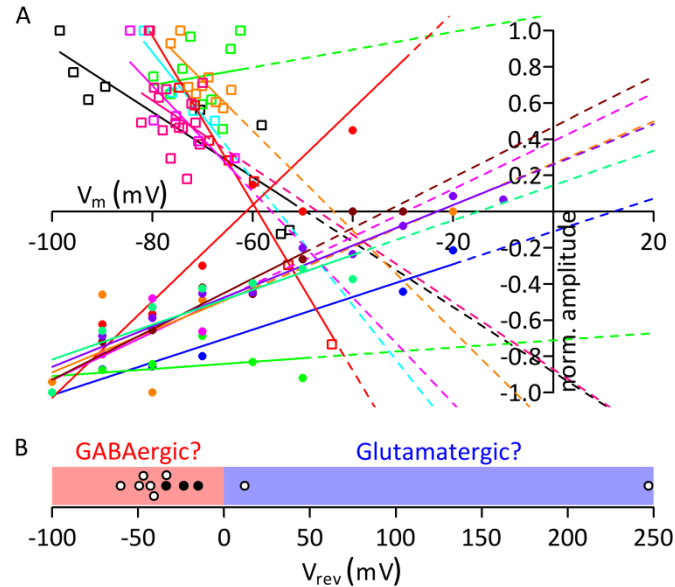
Figure 3.13: **Reversal Potential (V$_{rev}$)**. (**A**) Normalized postsynaptic potentials (□) and currents (●) plotted against the holding potential (voltage clamp) and the membrane potential (current clamp) just before the stimulus. Each color codes for one neuron. A linear regression (solid line) and its extrapolation (dashed line) are calculated for each neuron. The intersection with the abscissa indicates V$_{rev}$, the point at which there is no net flow of any current. (**B**) The distribution of per neuron average V$_{rev}$. The neurons are grouped in putative GABAergic and glutamatergic synapses based on the sign of V$_{rev}$. For the neurons indicated by filled circles I used 4 mM Cl$^-$ in the intracellular solution instead of 20.7 mM.

not systematically change with the distance between the site of the current's source and the soma (Figure 3.14 C).

As the "space-clamp" issue cannot explain the measurements of V$_{rev}$, I reduced the chloride content of the intracellular solution to 4 mM. This should shift V$_{rev}$ to more hyperpolarized potentials. However, this was not the case, as V$_{rev}$ in these three neurons was closer to 0 mV than for the other negative V$_{rev}$s (Figure 3.13 B).

Next, I employed immunohistological antibody stainings against VGAT and VGLUT-1, markers for GABAergic and glutamatergic synapses, respectively. If I truly stimulated GABAergic
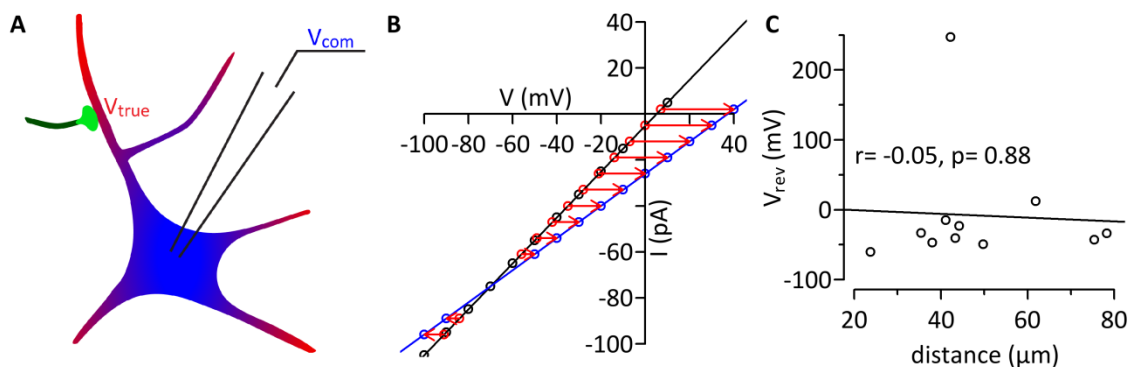
Figure 3.14: **Space-Clamp Issue**. (**A**) Within the neuron the command voltage (V$_{com}$, blue), controlled by the amplifier, drops to the naïve potential (red) as a function of the distance from the patch. The local membrane potential at the synapse is therefore not V$_{com}$, but V$_{true}$. (**B**) Assuming a model neuron and synapse (V$_{rest}$ of -70 mV, EPSC amplitude of -70 pA at V$_{rest}$, and V$_{rev}$ of 5 mV) without other conductances could yield the data in black. If the offset provided by V$_{com}$ is attenuated to 70 %, the amplitude of the EPSC measured at V$_{true}$ (red) would be plotted against V$_{com}$ (blue) and thus yield a higher V$_{rev}$ of 37.1 mV. (**C**) V$_{rev}$ does not correlate (Pearson correlation: r = -0.05, p = 0.88) with the distance between synapse and soma.

synapses, a proportion of the GFP-positive synapses should also be positive for the GABAergic synaptic marker VGAT. To this end, I binarized background and signal of both channels, i.e. GFP signal and antibody staining (Figure 3.15). From the binary image stacks I extracted for each synapse its volume (Figure 3.16) and its overlap, i.e. the percentage of the volume that is also positive for the antibody (Figure 3.17).

Overall all synapses take up a volume of $1.01 \pm 1.09 \, \mu m^3$ (mean ± width, n = 94847) as determined by a lognormal distribution fit on the histogram of all volumes of all stacks taken from all transcranially perfused animals (Figure 3.16). The median is: $1.91 \, \mu m^3$ and the
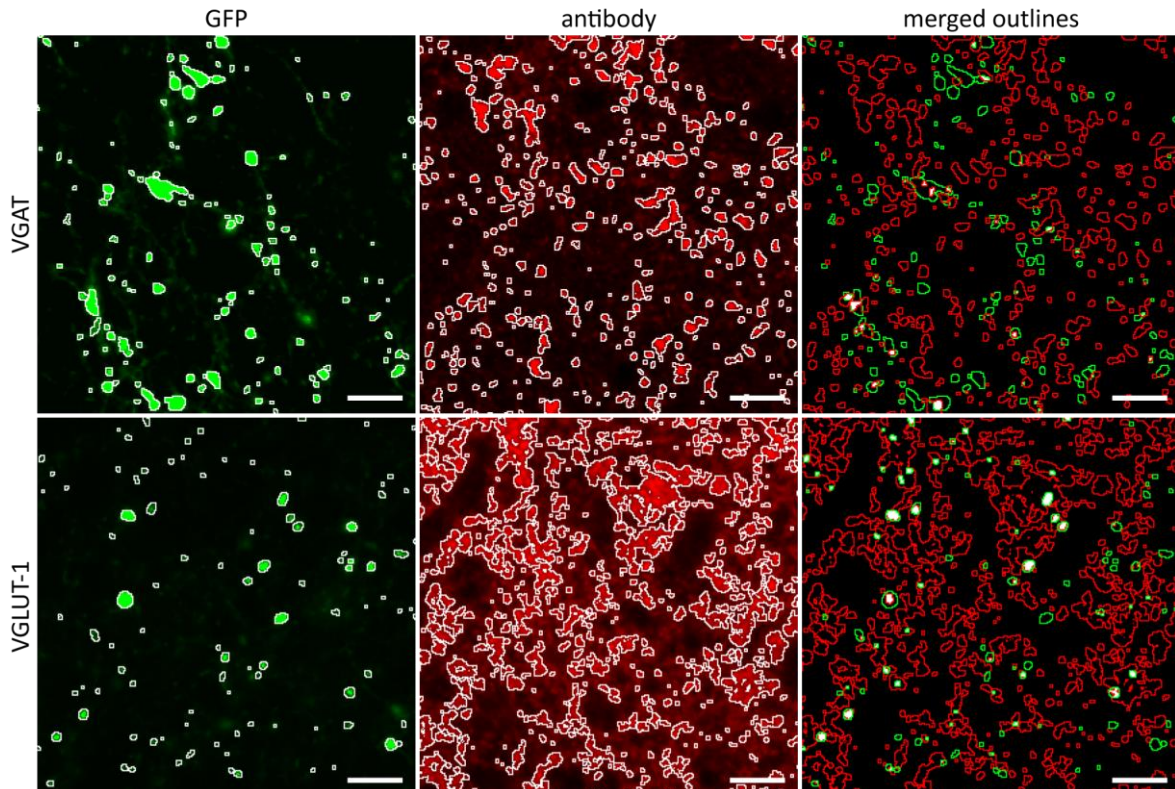
Figure 3.15: **Antibody Staining Against VGAT and VGLUT-1 in the MD With GFP-labeled Synapses From the PIR**. Upper row: single image plane from a stack of a staining against VGAT; lower row: same for staining against VGLUT-1. Left column: GFP, i.e. synapse, signal, the binary signal is outlined in white; middle column: antibody signal, the binary signal is outlined in white; right column: merged color matched outlines from GFP and antibody staining, the overlap is filled in white.
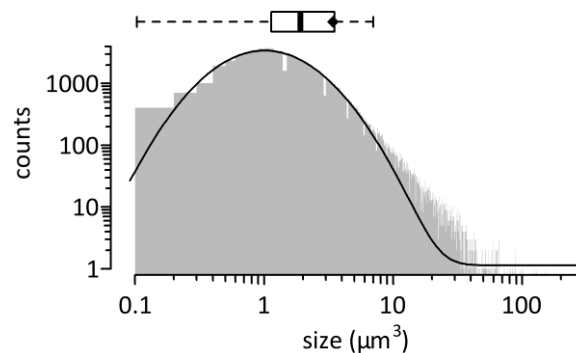
Figure 3.16: **Size Distribution of PIR-MD Synapses**. The histogram of all synapses (n = 94847) in $0.1 \, \mu m^3$ bins is fitted by a lognormal function (black line) with a mean of $1.01 \, \mu m^3$ and a width of $1.09 \, \mu m^3$. Above the histogram the same data is summarized in a boxplot. The boxplot edges spans from the 25 % to 75 % quartile. The median is indicated by the thick black line. The whiskers span 1.5 times the interquartile distance. The black diamond represents the arithmetic mean of all synapses.

average is $3.42 \pm 6.43~\mu m^3$ (Figure 3.16). The peak of the distribution is followed by a long tail of substantially larger synapses. Synapses from the immunohistological staining in slices first used for electrophysiological recordings have a smaller volume by a factor of 1.93. Therefore, they are excluded for the calculation of the average size above.

In order to quantify the percentage of synapses positive for either marker, individual synapses were scored as positive, if its overlap with the antibody reached the threshold in the range from 1 to 100 % (Figure 3.17). A 90°, 180°, and 270° rotation of one channel served as a control for overlap by chance. GFP-positive synapses from the PIR do not stain positive for the VGAT antibody (Figure 3.17). Although a fraction of GFP-labeled synapses co-occurred with the signal of the VGAT antibody, the fraction is smaller than the respective control (Figure 3.17 B & C). This observation is true when thresholding the overlap at 8 % or higher. The difference is with 1.66 % the largest for an overlap threshold of 42 %. It is a different picture for VGLUT-1. The fraction of synapses, which are positive for the marker, is always larger than the corresponding control value (Figure 3.17 B & C). The difference for
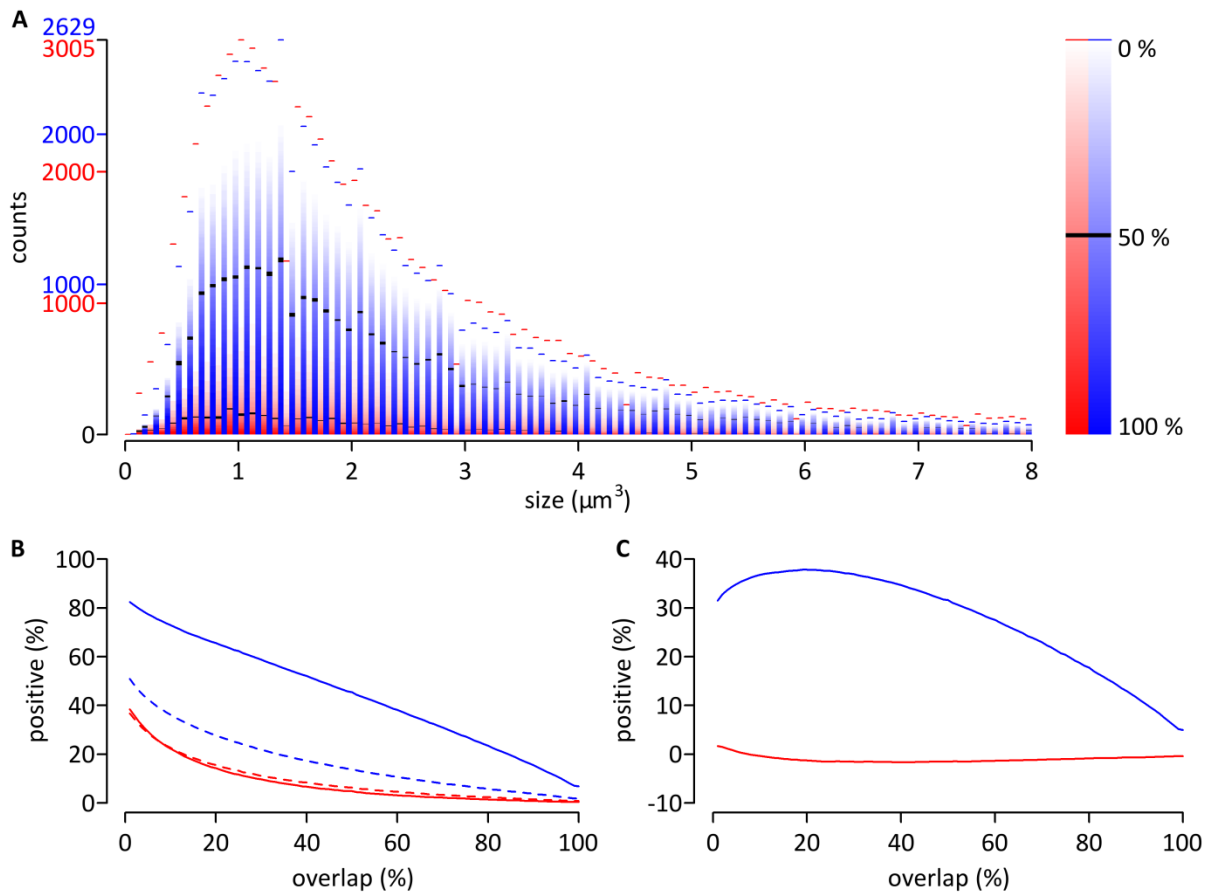
Figure 3.17: **Co-occurrence of Synaptic and Vesicular Neurotransmitter Marker**. (**A**) Histogram of sizes of synapses as measured in slices stained for VGAT (red) and VGLUT-1 (blue) cut off at $8~\mu m^3$. The volumes of from fixed acute slices were adjusted by the factor of 1.93 (see text). The height of the histograms is matched, thus the axis scale differently. The saturation of the color corresponds to the threshold (percentage of synaptic volume that is also positive for the antibody) used to score synapses as either positive or negative. To aid the visual interpretation the 50 % threshold is highlighted in black. A cap at the end of each bar indicates the total number of synapses in each bin ($0.1~\mu m^3$). (**B**) The percentage of positive synapses out of all synapses for a given threshold. The percentage of positive synapses is given by the solid line. The percentage for the controls (average of rotation by 90°, 180°, and 270°) is given by the dashed line. (**C**) The residual positive synapses after subtraction of the control.

the staining and the control is largest (37.85 %) when thresholding the overlap at 20 %. For a threshold of 1 % the difference is 31.52 % and for 100 % overlap it is 4.93 %.

In summary, the change of intracellular chloride concentration did not shift V_{rev} to even more hyperpolarized potentials. The labeled synapses do not co-occur with a GABAergic synaptic marker, but with VGLUT-1, a marker for a subpopulation of glutamatergic synapses. Therefore, the PIR-MD synapses are not GABAergic and the measured synapses do not have to be split into different groups.

4 Discussion

In this study, I investigated the synaptic distribution and the synaptic transmission characteristics of the synapses connecting piriform cortical axons with mediodorsal thalamic neurons. This is the first functional description of the single synaptic physiology of a paleocorticothalamic projection. As the age of the animal did not have an effect on the measured EPSC parameters (Figure 3.8), I conclude that I investigated on the mature synapse. In order to functionally describe the PIR-MD synapse, did I employ electro-physiological recordings with single synapse stimulation, electron microscopic investigations, and immunohistochemistry.

For electrophysiological experiments the synapses of interest were labeled via stereotaxically delivered AAV-mediated gene transfer of synaptophysin-GFP fusion proteins into the PIR harboring the projection neurons. In the thalamic target area, GFP-labeled fluorescent vesicles marked the position and size of the synapses. The experimental difficulties lie in the successful and stable stimulation of single synapses. In many cases the patched neurons seemed to be contacted by labeled synapses, but often they either do not respond to the electric stimulation or are connected to other nearby dendrites. In total in only 31 cases the stimulation was sufficient to start the stimulation protocol. 20 out of theses 31 recordings had to be dismissed during later analysis. The 31 recordings stemmed from 130 sacrificed animals

Using the same gene transfer method a synaptophysin-pHluorin fusion protein was expressed in PIR neurons. After photooxidation in perfusion-fixed tissue the sample was prepared for electron microscopy. Here, the serial sectioning of many slices in a row and subsequent screening of the tissue limits the throughput. The inspected tissue contained 3 full giant synapses, 2 more partially, 1 small synapse and 12 axo-axonal synapses.

4.1 Distribution of Synapses Along the Somato-Dendritic Axis

Alongside the ultrastructure of the PIR-MD synapses, also their distribution along the dendrites is of interest. PIR-MD synapses are on average evenly distributed across the dendritic tree of the MD neurons, as the synaptic count is independent of the radial distance of the synapse and the center of mass of the neuron in the range of 20 - 70 μm (Figure 3.4A). However, 4 out of 9 neurons had their peak number of synapses within the range of 30 μm. The remaining 5 did not display this peak. The initial peak could reflect the finding that the RL-type synapses are primarily located on primary dendrites, while the number of RS-type terminals increases on higher order dendrites (Kuroda et al., 1992b). Therefore, I looked at the size distribution of the synapses grouped by their distance to the soma (Figure 3.4B). The closer synapses are on average smaller than the ones further away, which contradicts the

finding by Kuroda and colleagues, assuming that the type of synapse is reflected in the fluorescent microscopic apparent size. However, the discrepancy between light and electron microscopic identification of the synapses will be discussed below.

I also analyzed synaptic sizes in a larger field of view in perfusion-fixed tissue samples (Figure 3.16). If both, modulators and driver synapses, are present and their volumes deviate enough to allow a clear separation based on size, the histogram should have two distinct peaks. However, the distribution is continuous with a single peak at around 1 μm^3. A spherical synapse with 1 μm^3 would have a diameter of 1.2 μm and a maximal cross section of 1.13 μm^2. This does not fit to either group described by Kuroda and Price (1991), who found that RS-boutons to have diameter of <1 μm and RL-boutons 2 - 3 μm on their short axis, as measured in EM sections of rat MD. Similarly, does it not match the described area of cross sections (RS: 0.34 ± 0.1 μm^2 and RL: 2.15 ± 0.6 μm^2) (Çavdar et al., 2011) or the diameter described for RS-terminals (0.82 ± 0.22 μm) (Négyessy et al., 1998), both studies also performed on EM sections of rat MDs. Llano and Sherman (2008) have reported that the auditory corticothalamic projections in mice possess two groups of synapses separate at 2 μm with a small gap between the distribution of <2 μm and >2 μm synapses in light microscopy. No such gap was apparent here. One limitation of fluorescence microscopy is to determine the edge of the signal correctly. Minor differences in thresholding can change the apparent volume of a fluorescent structure. Additionally, particularly weak fluorescent objects may easily be lost in the noise. The continuous histogram with a single peak at intermediate volumes probably stems from a mixed population. In fact, it was also previously known and was confirmed here that synapses from the PIR in MD can be of either type. The numbers for the proportion of RS to RL-types range from predominantly RL-types (Kuroda and Price, 1991) and in a second study up to 64 % RS-types (Kuroda et al., 1992b). Kuroda and Price (1991) also reported intermediate terminal cross section areas (out of 50 terminals: 9 small (<1 μm), 14 medium (≤1 and ≤2 μm), and 27 large (>2 μm) ones). In conclusion, the size of the synapse in confocal fluorescent microscopy is a poor criterion to differentiate between modulators and drivers in MD, unless one looks at very large terminals, which are highly likely to be RL-boutons. The inability to differentiate the types by size was also described for macaque monkeys (Rovó et al., 2012).

4.2 3D Ultrastructure of PIR-MD Synapses

Špaček and Lieberman (1974) were the first to describe the 3D-structure from serial sections of synaptic glomeruli of the rat somatosensory thalamus. They also found the complex architecture of excrescences growing into the presynaptic bouton. Their reconstructed boutons could contain up to 10 synaptic contacts per excrescence. The mitochondria make up a smaller proportion of the lumen, i.e. only 11.6 % instead of the 21.5 ± 2.3 % found here. However, it is not clear if their percentage is proportional to the presynaptic volume, as it is here, or proportional to the combined presynaptic and postsynaptic excrescences volume. Besides representing a true difference, it could also arise from different fixation and processing methods.

Budisantoso and colleagues (2012) found a similar 3D organization at the retinogeniculate synapse. Multiple protrusions grow out of the dendrite to enlarge the contact surface between bouton and dendrite. By use of the freeze-fracturing method, they quantified 27 ± 2.7 synaptic contacts per bouton. They concluded that this comes at the expense or as a feature of the short-term depression, as the surplus glutamate cannot rapidly diffuse and is not cleared away, but will enhance AMPA receptor desensitization. On the contrary, STD was unaltered at the L5B-POm synapse by kynurenic acid, a low affinity antagonist for AMPA receptors, which reduces desensitization and saturation (Groh et al., 2008). Final proof for the major mechanism determining STD at the PIR-MD synapse can only be obtained experimentally. However, experimental proof was not feasible due to the limited yield of the electrophysiological experiments.

4.3 Axo-Axonal Synapses on PIR-Axons in the MD

As a surprise I found axo-axonal synapses. This type of synapse has not been described for the MD previously. Kuroda and colleagues (1991; 1998) explicitly state that they only found axodendritic, axospinous, and axosomatic synapses. Others do not mention axo-axonal contacts either (Çavdar et al., 2011; Kuroda et al., 1992b; Ray et al., 1992). In fact, there are no reports of chemical synapses on axons at locations other than the axon hillock or near axon terminals. There are many reports of synaptic contacts on other synaptic boutons (to name a few: Ehinger et al., 1970; Gobel and Dubner, 1969; Rosenstein and Leure-Dupree, 1977; Smith and Marzban, 1998), synapses on the axon initial segment (Inan and Anderson, 2014; Pinault et al., 1997) also in PIR (Wang and Sun, 2012), and electric synapses / gap junctions between axons (Maex and De Schutter, 2007; Schmitz et al., 2001; Traub et al., 1999), but none on chemical synapses onto the axon itself.

The targeted axons were identified by their darkened mitochondria. A strong indicator that the neurite originates in the injection area, at a distance far enough to exclude viral gene transfer directly to MD relay neurons. The structures include some membranous compartments which could be endosomes or part of the ER. This would point rather to a dendritic than to an axonal identity. However, the identification of neurites based on the ultrastructure is difficult and unreliable. Therefore the data supports the interpretation that within the MD axo-axonal synapses on intermediate axonal segments exist, but a false positive identification of unspecific reaction product cannot formally be excluded. Rodents are an exception to the observation that driver synapses form a triade conformation with a GABAergic terminal and the dendrite within a glomerulus (Sherman and Guillery, 2006). It is tempting to speculate whether these axo-axonal synapses function in a similar manner, just on the axon rather than the bouton, but the data does not allow to draw firm conclusions.

In conclusion of the image data analysis, does the synaptic size in confocal fluorescence microscopy not predict the synaptic identity. Therefore, the distribution of the two types of synapses cannot be differentiated and analyzed separately. Individual neurons may display a very different distribution pattern with the highest number of synapses in close proximity of the soma, highest synaptic count on distal dendrites, or a homogeneous one. The average of

the heterogeneous distribution pattern is homogenous across the distance range of 20 - 70 µm. In electron microscopy I focused on the description of RL-type, i.e. driver, synapses. The PIR-MD RL-synapse shows the typical morphological characteristics as for other synapses of the same type. Apparently a new type of axo-axonal synapses exists in the MD of mice, but this finding needs to be confirmed with additional experiments. Their function also remains to be investigated.

4.4   Basic MD Relay Neuron Characterisitcs

The recorded passive and active parameters of MD neurons fall into the normal, physiological range determined for neurons in various brain regions: V_{rest}: -75.8 ± 7.1 mV, R_{mem}: 192.1 ± 68.9 MΩ, V_{thres}: -50.7 ± 4.8 mV, AHP: -14.2 ± 2.8 mV (compare http://www.neuroelectro.org/, a collection of parameters across many different neuronal types and in particular thalamic relay neurons) and can therefore be considered intact and healthy.

Although the neurons at which a synaptic stimulation was successfully recorded had a significantly lower input resistance, the functional relevance and significance of this effect remains to be determined in a larger experimental sample. Theoretically, the low input resistance could be a marker for one of the two neuron types (stellate and fusiform) described by Kuroda and colleagues (1992a, 1998), which would also need to be selectively targeted by PIR axons to yield this result. However, the overall distribution of R_{mem} does not allow to postulate the existence of two distinct neuron populations in the MD.

4.5   PIR-MD Synapses Are Not GABAergic

I measured the reversal potential (V_{rev}) of the evoked monosynaptic EPSCs. The apparent V_{rev} is very variable and deviates often enough from the expected value (~0 mV) of glutamate-evoked sodium-carried currents to investigate the possibility of having stimulated a chloride-based conductance. Several findings oppose this notion.

First of all, the currents are quite fast (rise time: 0.54 ± 0.08 ms, tau: 2.25 ± 0.97 ms) which is often considered a hallmark of glutamatergic synapses, although GABAergic synapses may display similar kinetics (Bartos et al., 2007). Secondly, the change of intracellular Cl^- concentration does not yield the expected lower V_{rev}, but a higher one. The current is therefore not carried by chloride ions. Thirdly, VGAT, a marker for GABAergic synapses, does not co-occur with the synaptic-GFP marker. Additionally, no GABAergic projection neurons to the MD were found in PIR (Kuroda and Price, 1991; Ray et al., 1992; Young et al., 1984). I cannot formally exclude the possibility that some projection neurons from the ventral pallidum, which are known to be at least partially GABAergic (Young et al., 1984), confine the results. However, in light of the evidence arguing against GABAergic synapses above, the confinement by ventral pallidal projections is considered unlikely.

I also investigated if the space clamp problem might introduce a systematic error. The model yields the same results as it has been described before by Calvin (1969) and Williams & Mitchell (2008), namely that the predicted error has the opposite sign of the observed

deviation. Furthermore, V_{rev} does not correlate with the distance between the current source and the soma. Space clamp problems can thus not explain the data.

Although V_{rev} was extrapolated with the assumption of a linear relationship between current and potential, when in fact the channels are slightly rectifying (e.g. Groh et al., 2008), the introduced error is assumed to be minimal. If anything, a correction of the error would yield more a depolarized V_{rev}, away from the chloride reversal potential.

In summary, I conclude that the stimulated synapses were not GABAergic, but triggered by another neurotransmitter as will be discussed below.

4.6   The PIR-MD Primary Neurotransmitter

The primary neurotransmitter of projection neurons from the PIR to MD is not known, yet. I could exclude GABA as the principal neurotransmitter (see above). Several other candidates have been proposed: neurotensin (Inagaki et al., 1983; Kuroda et al., 1991) and glutamate (Ray et al., 1992).

Inagaki et al. (1983) found reduced immunoreactivity against neurotensin in the MD exclusively after lesioning PIR. However, they could not find retrogradely labeled neurons that also exhibited neurotensin immunoreactivity. Kuroda and colleagues (1991) found neurotensin in RL-type boutons, which may only stem from PIR neurons, according to a follow up study (Kuroda et al., 1992b). Neurotensin interacts with 3 known receptors (NTS1-3) (Cáceda et al., 2006). All are metabotropic and thus unsuitable to explain the fast kinetics of the EPSC (Cáceda et al., 2006). Furthermore neurotensin is most often investigated in association with the dopaminergic system. But there are a few reports on the up or down regulation of EPSC amplitude at glutamatergic synapses (Bose et al., 2015; Ferraro et al., 2008; Yin et al., 2008). Nevertheless neurotensin is most likely a neuromodulator and cannot explain the current results.

Ray and colleagues (1992) put forward evidence that the primary neurotransmitter may be glutamate. Glutamate binds to the ionotropic NMDA, AMPA, and kainate receptors and metabotropic mGluRs. Several other giant synapses in the thalamus have already been thoroughly tested for their kinetics and the contributions of NMDA and AMPA receptors both in mice and in rats (Groh et al., 2008; Seol and Kuner, 2015; Urra Quiroz, 2014). The values are summarized in Table 4.1. The kinetics match across different species and

Table 4.1: **Comparison with other giant synapses**.

synapse	species	20 - 80 % rise time [ms]	decay constant [ms]	amplitude [pA]	RRP [pA]	P_{rel} [%]	recovery constant [ms]	steady-state STD at 50 Hz [%]
PIR-MD	mouse	0.54 ± 0.08	2.25 ± 0.97	391 ± 522	862 ± 947	50 ± 22	1340 ± 290	18
PR5-VPm[a]	rat	0.41 ± 0.03	1.92 ± 0.24	990 ± 240	5100 ± 1300	20		12[+]
L5B-POm[b]	mouse	0.8 ± 0.05	3.5 ± 0.2	257 ± 33	448 ± 46	51 ± 7	1: 15 ± 4 2: 195 ± 187	20[+]
L5B-POm[c]	rat	0.43 ± 0.17	1.23 ± 0.27	3330 ± 1450	4100 ± 1700	80 ± 9	1: 27 2: 423	14 ± 7

RRP: readily releasable pool, P_{rel}: release probability, [a]= (Urra Quiroz, 2014), [b]= (Seol and Kuner, 2015), [c]= (Groh et al., 2008), [+]= inferred from figure

synapses. All three synapses were pharmacologically tested for NMDA and non-NMDA contribution to the naïve current. In all cases the majority of the total current was conducted by AMPA receptors and only to a smaller degree by NMDA receptors.

This also agrees with the finding that around 30 % of all PIR synapses were positive for vGLUT-1. The remaining synapses may express vGLUT-2, which is also, but to a lower extend, expressed in PIR (Nakamura et al., 2005). If paleocorticothalamo projection neurons have a higher probability to express vGLUT-2 is unknown. Alternatively, another transmitter system cannot be excluded. Also the immunostaining and post-hoc segmentation may not be sensitive enough and resulted in a high false-negative rate.

The slower recovery (Table 4.1) constant may be explained by the different stimulation protocols used. Here the readily releasable pool was depleted by stimuli trains, while the other reported values are inferred from paired pulse stimulation protocols (Groh et al., 2008; Seol and Kuner, 2015; Urra Quiroz, 2014).

For all these reasons, I conclude that the PIR-MD synapse functions via glutamate release. A formal proof could be obtained by pharmacological means. A treatment with 6-cyano-7-nitroquinoxaline-2,3-dione (CNQX), an AMPA receptor antagonist, would proof the involvement of AMPA receptors and could also segregate the contributions of the AMPA and NMDA receptors. This pharmacological approach was hampered by the low yield of the electrophysiological experiments.

4.7   Do PIR-MD Synapses Have the Drive?

To answer that question, one needs to compare them with other synapses defined as drivers, in parameters defined by Sherman and Guillery (2006).

First of all, driver synapses need to be large, i.e. RL-type, with multiple contacts. Multiple contacts facilitate large postsynaptic current, as more quanta can be released simultaneously. Although the number of contacts could not be determined, the 3D-reconstructions from EM images clearly show the hallmarks of RL-type synapses. This is in agreement with previous reports (Kuroda et al., 1992b; Kuroda and Price, 1991; Ray et al., 1992).

Secondly, driver synapses are supposed to have large EPSCs, are glutamatergic, and activate ionotropic receptors. Previous reports suggested either neurotensin or glutamate as the principal neurotransmitter. The measured EPSC kinetics and the comparison with other driver synapses (see above) indicates that the PIR-MD synapse is glutamatergic and probably acts on fast ionotropic receptors. The amplitude of the EPSC is on average larger than for the L5B-POm synapse in mice (Seol and Kuner, 2015), but smaller than in rats (Groh et al., 2008). However there is no data on any other species' PIR-MD synapse for direct comparison available.

Thirdly, driver synapses show paired-pulse depression. Here, not only paired pulses were recorded, but trains of stimuli. The EPSC amplitude depresses in a stimulation frequency dependent manner, as it has been described for other driver synapses (Budisantoso et al.,

2012; Groh et al., 2008; Li et al., 2003; Reichova and Sherman, 2004; Seol and Kuner, 2015; Turner and Salt, 1998; Urra Quiroz, 2014).

Fourthly, driver synapses exhibit a high release probability. The PIR-MD synapses match release probabilities (P_{rel}) of L5B-POm synapses for mice, but have a lower P_{rel} than for L5B-POm in rats (Groh et al., 2008; Seol and Kuner, 2015). PIR-MD P_{rel} is higher than for peripheral auditory inputs (PR5-VPm) in rats (Urra Quiroz, 2014).

In conclusion, the PIR-MD synapses fulfill many characteristics of the driver model.

4.8   Postsynaptic Activity

The term "driver" suggests that these synapses are strong enough to evoke postsynaptic action potentials. However, only in a single case was the postsynaptic current strong enough to reliably evoke action potentials. That is in only 12.5 % of all analyzed cells. This percentage is lower than in other reports. Seol and Kuner (2015) report that 21 % of all EPSCs were large enough to trigger postsynaptic spikes. In case of the retinogeniculate synapse 46 ± 16 % of retinal action potentials are followed by a thalamic action potential in rhesus monkey (Sincich et al., 2007). Budisantoso et al. (2012) found that large EPSCs always trigger postsynaptic action potentials, while small (<500 pA) EPSCs fail more often as the membrane potential decreases. For others the probability is not explicitly stated or apparent from the data, but it is obvious that also not all EPSCs trigger action potentials (Li et al., 2003; Reichova and Sherman, 2004; Turner and Salt, 1998).

The postsynaptic action potential generation is a response property of the postsynaptic neuron. It is therefore worthwhile to have a look at some of the relay neuron characteristics. Mainly the I_T currents shape the responses at low membrane potentials. It is well established that thalamic relay neurons express low-threshold activated calcium-channels (Ca_v3). The exact expression profiles of the three channels ($Ca_v3.1$-3.3) are not unequivocally determined, but the reports have in common that $Ca_v3.1$ is the major somatic channel (Liu et al., 2011; McKay et al., 2006; Talley et al., 1999). A comparison with the channel kinetics also indicates that $Ca_v3.3$ and $Ca_v3.2$ are too slow to yield the measured currents (Chemin et al., 2002). A $Ca_v3.1$ knock-down study in the POm clearly showed that the postsynaptic spiking at low membrane potentials is eliminated, while at higher potentials the "tonic" relay function is unperturbed (Seol and Kuner, 2015). The same study also establishes that the EPSC amplitude and number of postsynaptic action potentials does not correlate. It is therefore the interplay of presynaptic transmitter release and postsynaptic receptor and channel profile that determines the input-output function.

As the term "driver" might be misleading, in regard of the probability of evoked action potentials, I suggest to take up the updated terminology of "class I" (previously driver) and "class II" (previously modulator) synapses. Sherman and Guillery (2011) originally introduced the new nomenclature to extend the concept of thalamic drivers and modulators to the cortex, but a number-based nomenclature also allows the easy addition of yet to be found and defined classes of synapses to the system. Renaming drivers to class I and modulators to class II is less intuitive, but circumvents some false assumption.

4.9   Function of Transthalamic Connection of PIR and PFC via MD

The exact function of the transthalamic route for the corticocortical communication is not well understood - neither for the PIR-MD-PFC pathway, nor for any other cortico-thalamo-cortical circuit.

First-order, i.e. primary sensory, nuclei prime the information for cortical processing. It is more than just a mere selection process, as afferent information maybe be amplified in a burst or linearly represented in tonic mode. This mechanism has been postulated to underlie attention. As thalamic relay neurons in higher-order nuclei function the same way, it is obvious to postulate the same function - attention - for nuclei like the MD.

Supportive data comes from the observation that the effective connectivity in humans between PIR to MD and MD to PFC increases, selectively during odor attention tasks, while all other connections were not significantly altered (Plailly et al., 2008). Keller (2011) came to a different conclusion, as, according to the author, attention is more likely to happen either at the level of the olfactory bulb or the PIR. The author proposed that the connection to MD is required to coordinate the shift of attention between olfaction and other sensory modalities.

Theyel at al. (2010) have put forward yet another model. Here the cortico-thalamo-cortical circuit serves as a reliable information transfer system, which profits from the thalamic intermediate processing. Although the transthalamic route needs to cover longer axonal distances and gap an additional synapse, the processing speed may be not much slower (Salami et al., 2003). To my knowledge there is no direct data on the different latencies for direct and indirect corticocortical communication. Therefore, ideas whether corticocortical efferents prime the secondary cortical areas for transthalamic input, wheather it is the other way around, or whether the system functions as a coincidence detector, are purely speculative.

The here presented results clearly indicate that most driver synapses are by themselves not sufficient to evoke action potentials in the MD. Assuming that the EPSC amplitude is on average 51 % or 19 % of the minimal required current to evoke an action potential, as determined by EPSC-shaped current injections, at least 2 or 5 synapses need to be simultaneously coactive. On average there are about 5 PIR driver synapses per dendrite (Kuroda et al., 1992b). This may suggest that multiple inputs need to be integrated at the dendrite or soma. In this scenario, the MD neurons would function as an integrative station rather than a mere relay for information.

4.10   Outlook

The functional relevance of the PIR-MD connection may only be assessed in well-designed behavioral tasks including specific perturbations to the system. As MD lesion studies often seemed to have a subtle effect on olfactory related learning tasks (Rousseaux et al., 1996; Sapolsky and Eichenbaum, 1980; Slotnick and Kaneko, 1981; Slotnick and Risser, 1990), more experiments will have to be conducted. Additionally MD lesions not only perturb the PIR-

MD-PFC connection, but also the reciprocal connections between PFC and MD. This close interlinkage between MD and PFC has been found to be involved in various cognitive tasks (for a review see: Mitchell and Chakraborty, 2013). This circumstance complicates the interpretation of the data. One aspect that however has not been investigated in MD lesioned mice or rats so far, is whether attentional shifts between the sensory modalities is impaired specifically when shifting to or from olfaction towards another modality; a paradigm that could be designed without having to refine the perturbation. But ideally one would target specifically the PIR-MD connection without interference of any other system, which is not yet possible.

Also *in vivo* electrophysiological studies could provide valuable insights. In a simple operant-based reversal-learning task, single unit MD activity phase-locks best with PFC field potentials 20 ± 1.4 ms later, i.e. the MD activity leads the PFC activity (Parnaudeau et al., 2013). A similar parallel recording during olfaction-related tasks could surely be a milestone in understand the circuitry.

Furthermore, the identified axo-axonal synapses will have to be verified by conducting additional experiments, preferentially including different species, before a rigid conclusion can be drawn.

5 Acknowledgements

First of all, I would like thank Prof. Dr. Thomas Kuner for the opportunity to write my doctoral thesis in his lab, the freedom to explore anything that came to my mind, and all his advice.

All experiments would not have been possible without the support of various people. The following list is in no particular order and does not reflect nuances of gratitude. Michaela Kaiser cloned the constructs used for this thesis and various more. Claudia Kocksch produced the virus, without which the experiments would not have been possible. Marion Schmitt spent tons of hours at the slicer for me, freeing me to work on other stuff. All three did a great job of keeping the lab running in general. Heinz Horstmann and Inge Frommer put in the effort to process the tissue and acquire the EM images. Daniel Nunes introduced me to the olfaction behavior, which unfortunately does not find mentioning in the thesis. Hongwei wrapped his Matlab codes around some of the confocal images. Christoph Körber was usually the first to have to deal with my questions and shared his experience. Denise and Sabrina were always around for good fun in- and outside the lab. Marcel Smykalla took some of the planed experiments of my back. Janine Reinert gave helpful comments on the manuscript. But my thanks extend to all members of the lab and the department that are not explicitly mentioned for the overall working experience.

I also want to take the opportunity to thank Prof. Dr. Hilmar Bading and Dr. Johann Bollmann for their time, the discussion, and their suggestions during the annual TAC-meetings.

Life would be boring without friends – Life-long friends, friends made during my studies at university and "new" friends in Heidelberg alike. Please all feel thanked.

My family always supported me unconditionally to achieve all my goals. They never doubted my decisions and helped whenever possible.

The biggest "thanks" goes to my own little family. Svenja, thank you for being who you are. Unborn "Randale Ralf", I am really looking forward to finally meet you.

6   Abbreviations

AAV	adeno-associated virus
AHP	afterhyperpolarization
ATP	adenosine-5'-triphosphate
DAB	3,3'-Diaminobenzidine
DMEM	dulbecco'2 minimal essential medium
eGFP / GFP	(enhanced) green fluorescent protein
EGTA	ethylene glycol-bis(2-aminoethylether)-N,N,N',N'-tetraacetic acid
EM	electron microscopy
EPSC	excitatory postsynaptic current
EPSP	excitatory postsynaptic potential
FCS	fetal calve serum
GABA	γ-aminobutyric acid
HBS	HEPES buffered solution
HEK	human embryonic kidney
HEPES	4-(2-hydroxyethyl)-1-piperazineethanesulfonic acid
I_T	low-threshold activated calcium-currents / T-type currents
LGN	lateral geniculate nucleus of the thalamus
LTS	low-threshold spike
MD, MDl, MDc, MDm	mediodorsal thalamus (lateral / central / medial)
NA	numerical aperture
NGS	normal goat serum
ORN	olfactory recepter neuron
PBS	phosphate buffered saline
PFA	para-formaldehyde
PFC	prefrontal cortex
PIR	piriform cortex
POm	posteriomedial nucleus of the thalamus
PSD	postsynaptic density
R_{mem}	membrane access resistance
RRP	readily releasable pool
SD	standard deviation
SEM	standard error of the mean
STD	short-term depression
vGAT	vesicular GABA transporter
vGLUT-1	vesicular glutamate transporter 1
V_{rest}	membrane resting potential
V_{rev}	reversal potential
V_{thres}	action potential threshold
P_{rel}	release probability

7 References

Arcelli, P., Frassoni, C., Rregondi, M. C., Biasi, S. D., and Spreafico, R. (1997). GABAergic Neurons in Mammalian Thalamus: A Marker of Thalamic Complexity? *Brain Res. Bull.* 42, 27–37. doi:10.1016/S0361-9230(96)00107-4.

Barry, P. H., and Lynch, J. W. (1991). Liquid junction potentials and small cell effects in patch-clamp analysis. *J. Membr. Biol.* 121, 101–117. doi:10.1007/BF01870526.

Bartos, M., Vida, I., and Jonas, P. (2007). Synaptic mechanisms of synchronized gamma oscillations in inhibitory interneuron networks. *Nat. Rev. Neurosci.* 8, 45–56. doi:10.1038/nrn2044.

Bar-Yehuda, D., and Korngreen, A. (2008). Space-Clamp Problems When Voltage Clamping Neurons Expressing Voltage-Gated Conductances. *J. Neurophysiol.* 99, 1127–1136. doi:10.1152/jn.01232.2007.

Bose, P., Rompré, P.-P., and Warren, R. A. (2015). Neurotensin enhances glutamatergic EPSCs in VTA neurons by acting on different neurotensin receptors. *Peptides* 73, 43–50. doi:10.1016/j.peptides.2015.08.008.

Budisantoso, T., Matsui, K., Kamasawa, N., Fukazawa, Y., and Shigemoto, R. (2012). Mechanisms Underlying Signal Filtering at a Multisynapse Contact. *J. Neurosci.* 32, 2357–2376. doi:10.1523/JNEUROSCI.5243-11.2012.

Cáceda, R., Kinkead, B., and Nemeroff, C. B. (2006). Neurotensin: Role in psychiatric and neurological diseases. *Peptides* 27, 2385–2404. doi:10.1016/j.peptides.2006.04.024.

Cain, S. M., and Snutch, T. P. (2010). Contributions of T-type calcium channel isoforms to neuronal firing. *Channels* 4, 475–482. doi:10.4161/chan.4.6.14106.

Cain, S. M., and Snutch, T. P. (2013). T-type calcium channels in burst-firing, network synchrony, and epilepsy. *Biochim. Biophys. Acta BBA - Biomembr.* 1828, 1572–1578. doi:10.1016/j.bbamem.2012.07.028.

Calvin, W. H. (1969). Dendritic synapses and reversal potentials: Theoretical implications of the view from the soma. *Exp. Neurol.* 24, 248–264. doi:10.1016/0014-4886(69)90018-1.

Çavdar, S., Hacıoğlu, H., Şirvancı, S., Keskinöz, E., and Onat, F. (2011). Synaptic organization of the rat thalamus: a quantitative study. *Neurol. Sci.* doi:10.1007/s10072-011-0606-4.

Chemin, J., Monteil, A., Perez-Reyes, E., Bourinet, E., Nargeot, J., and Lory, P. (2002). Specific contribution of human T-type calcium channel isotypes (α1G, α1H and α1I) to neuronal excitability. *J. Physiol.* 540, 3–14. doi:10.1113/jphysiol.2001.013269.

Coulter, D. A., Huguenard, J. R., and Prince, D. A. (1989). Calcium currents in rat thalamocortical relay neurones: kinetic properties of the transient, low-threshold current. *J. Physiol.* 414, 587–604. doi:10.1113/jphysiol.1989.sp017705.

Courtiol, E., and Wilson, D. A. (2013). Thalamic olfaction: Characterizing odor processing in the mediodorsal thalamus of the rat. *J. Neurophysiol.* doi:10.1152/jn.00741.2013.

Courtiol, E., and Wilson, D. A. (2015). The olfactory thalamus: unanswered questions about the role of the mediodorsal thalamic nucleus in olfaction. *Front. Neural Circuits*, 49. doi:10.3389/fncir.2015.00049.

Datiche, F., and Cattarelli, M. (1996). Reciprocal and Topographic Connections Between the Piriform and Prefrontal Cortices in the Rat: A Tracing Study Using the B Subunit of the Cholera Toxin. *Brain Res. Bull.* 41, 391–398. doi:10.1016/S0361-9230(96)00082-2.

Dong, H. W. (2008). *The Allen Reference Atlas: A Digital Color Brain Atlas of the C57BL/6J Male Mouse.* Auflage: 1. Auflage. Hoboken, N.J: John Wiley & Sons.

Ehinger, B., Falck, B., and Sporrong, B. (1970). Possible axo-axonal synapses between peripheral adrenergic and cholinergic nerve terminals. *Z. Für Zellforsch. Mikrosk. Anat.* 107, 508–521. doi:10.1007/BF00335438.

Eichenbaum, H., Shedlack, K. J., and Eckmann, K. W. (1980). Thalamocortical Mechanisms in Odor-Guided Behavior. *Brain. Behav. Evol.* 17, 255–275. doi:10.1159/000121803.

Ferraro, L., Tomasini, M. C., Mazza, R., Fuxe, K., Fournier, J., Tanganelli, S., et al. (2008). Neurotensin receptors as modulators of glutamatergic transmission. *Brain Res. Rev.* 58, 365–373. doi:10.1016/j.brainresrev.2007.11.001.

Gobel, S., and Dubner, R. (1969). Fine structural studies of the main sensory trigeminal nucleus in the cat and rat. *J. Comp. Neurol.* 137, 459–493. doi:10.1002/cne.901370405.

Groenewegen, H. J. (1988). Organization of the afferent connections of the mediodorsal thalamic nucleus in the rat, related to the mediodorsal-prefrontal topography. *Neuroscience* 24, 379–431. doi:10.1016/0306-4522(88)90339-9.

Groh, A., de Kock, C. P. J., Wimmer, V. C., Sakmann, B., and Kuner, T. (2008). Driver or Coincidence Detector: Modal Switch of a Corticothalamic Giant Synapse Controlled by Spontaneous Activity and Short-Term Depression. *J. Neurosci.* 28, 9652 –9663. doi:10.1523/JNEUROSCI.1554-08.2008.

Guido, W., Lu, S.-M., Vaughan, J. w., Godwin, D. W., and Sherman, S. M. (1995). Receiver operating characteristic (ROC) analysis of neurons in the cat's lateral geniculate nucleus during tonic and burst response mode. *Vis. Neurosci.* 12, 723–741. doi:10.1017/S0952523800008993.

Guido, W., and Weyand, T. (1995). Burst responses in thalamic relay cells of the awake behaving cat. *J. Neurophysiol.* 74, 1782–1786.

Herbert, A. D., Carr, A. M., and Hoffmann, E. (2014). FindFoci: A Focus Detection Algorithm with Automated Parameter Training That Closely Matches Human Assignments, Reduces Human Inconsistencies and Increases Speed of Analysis. *PLoS ONE* 9, e114749. doi:10.1371/journal.pone.0114749.

Horstmann, H., Vasileva, M., and Kuner, T. (2013). Photooxidation-Guided Ultrastructural Identification and Analysis of Cells in Neuronal Tissue Labeled with Green Fluorescent Protein. *PLoS ONE* 8, e64764. doi:10.1371/journal.pone.0064764.

Imamura, K., Onoda, N., and Takagi, S. F. (1984). Odor Response Characteristics of Thalamic Mediodorsal Nucleus Neurons in the Rabbit. *Jpn. J. Physiol.* 34, 55–73. doi:10.2170/jjphysiol.34.55.

Inagaki, S., Kubota, Y., Shinoda, K., Kawai, Y., and Tohyama, M. (1983). Neurotensin-containing pathway from the endopiriform nucleus and the adjacent prepiriform cortex to the dorsemedial thalamic nucleus in the rat. *Brain Res.* 260, 143–146. doi:10.1016/0006-8993(83)90776-X.

Inan, M., and Anderson, S. A. (2014). The chandelier cell, form and function. *Curr. Opin. Neurobiol.* 26, 142–148. doi:10.1016/j.conb.2014.01.009.

Inokuchi, A., Kimmelman, C. P., and Jr, J. B. S. (1993). Convergence of olfactory and nasotrigeminal inputs and possible trigeminal contributions to olfactory responses in the rat thalamus. *Eur. Arch. Otorhinolaryngol.* 249, 473–477. doi:10.1007/BF00168858.

Jones, E. G. (2009). Synchrony in the Interconnected Circuitry of the Thalamus and Cerebral Cortex. *Ann. N. Y. Acad. Sci.* 1157, 10–23. doi:10.1111/j.1749-6632.2009.04534.x.

Keller, A. (2011). Attention and olfactory consciousness. *Conscious. Res.* 2, 380. doi:10.3389/fpsyg.2011.00380.

Krettek, J. E., and Price, J. L. (1977). The cortical projections of the mediodorsal nucleus and adjacent thalamic nuclei in the rat. *J. Comp. Neurol.* 171, 157–191. doi:10.1002/cne.901710204.

Kuroda, M., López-Mascaraque, L., and Price, J. L. (1992a). Neuronal and synaptic composition of the mediodorsal thalamic nucleus in the rat: A light and electron microscopic golgi study. *J. Comp. Neurol.* 326, 61–81. doi:10.1002/cne.903260106.

Kuroda, M., Murakami, K., Kishi, K., and Price, J. L. (1992b). Distribution of the piriform cortical terminals to cells in the central segment of the mediodorsal thalamic nucleus of the rat. *Brain Res.* 595, 159–163. doi:10.1016/0006-8993(92)91468-T.

Kuroda, M., Murakami, K., Oda, S., Shinkai, M., and Kishi, K. (1993a). Direct synaptic connections between thalamocortical axon terminals from the mediodorsal thalamic nucleus (MD) and corticothalamic neurons to MD in the prefrontal cortex. *Brain Res.* 612, 339–344. doi:10.1016/0006-8993(93)91683-J.

Kuroda, M., and Price, J. L. (1991). Synaptic organization of projections from basal forebrain structures to the mediodorsal thalamic nucleus of the rat. *J. Comp. Neurol.* 303, 513–533. doi:10.1002/cne.903030402.

Kuroda, M., Price, J. L., and Ray, J. P. (1991). An ultrastructural study of neurotensin-like immunoreactive terminals in the mediodorsal thalamic nucleus of the rat. *Brain Res.* 548, 353–357. doi:10.1016/0006-8993(91)91149-U.

Kuroda, M., Sugiura, T., Shinkai, M., Murakami, K., Oda, S., and Kishi, K. (1993b). Synaptic organization and prefrontal corticothalamic termination in the mediodorsal thalamic nucleus of the cat. *J. Für Hirnforsch.* 34, 417–430.

Kuroda, M., Yokofujita, J., and Murakami, K. (1998). An ultrastructural study of the neural circuit between the prefrontal cortex and the mediodorsal nucleus of the thalamus. *Prog. Neurobiol.* 54, 417–458. doi:10.1016/S0301-0082(97)00070-1.

Leinwand, S. G., and Chalasani, S. H. (2011). Olfactory networks: from sensation to perception. *Curr. Opin. Genet. Dev.* 21, 806–811. doi:10.1016/j.gde.2011.07.006.

Li, J., Guido, W., and Bickford, M. E. (2003). Two Distinct Types of Corticothalamic EPSPs and Their Contribution to Short-Term Synaptic Plasticity. *J. Neurophysiol.* 90, 3429–3440. doi:10.1152/jn.00456.2003.

Liu, X.-B., Murray, K. D., and Jones, E. G. (2011). Low-threshold calcium channel subunit Cav3.3 is specifically localized in GABAergic neurons of rodent thalamus and cerebral cortex. *J. Comp. Neurol.* 519, 1181–1195. doi:10.1002/cne.22567.

Llano, D. A., and Sherman, S. M. (2008). Evidence for nonreciprocal organization of the mouse auditory thalamocortical-corticothalamic projection systems. *J. Comp. Neurol.* 507, 1209–1227. doi:10.1002/cne.21602.

Llinás, R., and Jahnsen, H. (1982). Electrophysiology of mammalian thalamic neurones in vitro. *Nature* 297, 406–408. doi:10.1038/297406a0.

Longair, M. H., Baker, D. A., and Armstrong, J. D. (2011). Simple Neurite Tracer: Open Source software for reconstruction, visualization and analysis of neuronal processes. *Bioinformatics*, btr390. doi:10.1093/bioinformatics/btr390.

Maex, R., and De Schutter, E. (2007). Mechanism of spontaneous and self-sustained oscillations in networks connected through axo-axonal gap junctions. *Eur. J. Neurosci.* 25, 3347–3358. doi:10.1111/j.1460-9568.2007.05593.x.

Maranto, A. R. (1982). Neuronal mapping: a photooxidation reaction makes Lucifer yellow useful for electron microscopy. *Science* 217, 953–955. doi:10.1126/science.7112109.

Mátyás, F., Lee, J., Shin, H.-S., and Acsády, L. (2014). The fear circuit of the mouse forebrain: connections between the mediodorsal thalamus, frontal cortices and basolateral amygdala. *Eur. J. Neurosci.* 39, 1810–1823. doi:10.1111/ejn.12610.

McKay, B. E., McRory, J. E., Molineux, M. L., Hamid, J., Snutch, T. P., Zamponi, G. W., et al. (2006). CaV3 T-type calcium channel isoforms differentially distribute to somatic and dendritic compartments in rat central neurons. *Eur. J. Neurosci.* 24, 2581–2594. doi:10.1111/j.1460-9568.2006.05136.x.

Mease, R. A., Krieger, P., and Groh, A. (2014). Cortical control of adaptation and sensory relay mode in the thalamus. *Proc. Natl. Acad. Sci.* 111, 6798–6803. doi:10.1073/pnas.1318665111.

Mitchell, A. S., and Chakraborty, S. (2013). What does the mediodorsal thalamus do? *Front. Syst. Neurosci.* 7, 37. doi:10.3389/fnsys.2013.00037.

Nakamura, K., Hioki, H., Fujiyama, F., and Kaneko, T. (2005). Postnatal changes of vesicular glutamate transporter (VGluT)1 and VGluT2 immunoreactivities and their colocalization in the mouse forebrain. *J. Comp. Neurol.* 492, 263–288. doi:10.1002/cne.20705.

Négyessy, L., Hámori, J., and Bentivoglio, M. (1998). Contralateral cortical projection to the mediodorsal thalamic nucleus: origin and synaptic organization in the rat. *Neuroscience* 84, 741–753. doi:10.1016/S0306-4522(97)00559-9.

Ollion, J., Cochennec, J., Loll, F., Escudé, C., and Boudier, T. (2013). TANGO: a generic tool for high-throughput 3D image analysis for studying nuclear organization. *Bioinformatics* 29, 1840–1841. doi:10.1093/bioinformatics/btt276.

Parnaudeau, S., O'Neill, P.-K., Bolkan, S. S., Ward, R. D., Abbas, A. I., Roth, B. L., et al. (2013). Inhibition of Mediodorsal Thalamus Disrupts Thalamofrontal Connectivity and Cognition. *Neuron* 77, 1151–1162. doi:10.1016/j.neuron.2013.01.038.

Pinault, D., Smith, Y., and Deschênes, M. (1997). Dendrodendritic and Axoaxonic Synapses in the Thalamic Reticular Nucleus of the Adult Rat. *J. Neurosci.* 17, 3215–3233.

Plailly, J., Howard, J. D., Gitelman, D. R., and Gottfried, J. A. (2008). Attention to Odor Modulates Thalamocortical Connectivity in the Human Brain. *J. Neurosci.* 28, 5257–5267. doi:10.1523/JNEUROSCI.5607-07.2008.

Powell, T. P., Cowan, W. M., and Raisman, G. (1965). The central olfactory connexions. *J. Anat.* 99, 791–813.

Price, J. L. (1973). An autoradiographic study of complementary laminar patterns of termination of afferent fibers to the olfactory cortex. *J. Comp. Neurol.* 150, 87–108. doi:10.1002/cne.901500105.

Price, J. L. (1985). Beyond the primary olfactory cortex: olfactory-related areas in the neocortex, thalamus and hypothalamus. *Chem. Senses* 10, 239–258. doi:10.1093/chemse/10.2.239.

Price, J. L., and Slotnick, B. M. (1983). Dual olfactory representation in the rat thalamus: An anatomical and electrophysiological study. *J. Comp. Neurol.* 215, 63–77. doi:10.1002/cne.902150106.

Ramcharan, E. J., Gnadt, J. W., and Sherman, S. M. (2000). Burst and tonic firing in thalamic cells of unanesthetized, behaving monkeys. *Vis. Neurosci.* 17, 55–62. doi:null.

Ray, J. P., and Price, J. L. (1990). Postnatal changes in the density and distribution of neurotensin-like immunoreactive fibers in the mediodorsal nucleus of the thalamus in the rat. *J. Comp. Neurol.* 292, 269–282. doi:10.1002/cne.902920209.

Ray, J. P., Russchen, F. T., Fuller, T. A., and Price, J. L. (1992). Sources of presumptive glutamatergic/aspartatergic afferents to the mediodorsal nucleus of the thalamus in the rat. *J. Comp. Neurol.* 320, 435–456. doi:10.1002/cne.903200403.

Reichova, I., and Sherman, S. M. (2004). Somatosensory Corticothalamic Projections: Distinguishing Drivers From Modulators. *J. Neurophysiol.* 92, 2185–2197. doi:10.1152/jn.00322.2004.

Rosenstein, J. M., and Leure-Dupree, A. E. (1977). Synaptic Organization of the external cuneate nucleus in the rat. *J. Comp. Neurol.* 175, 159–179. doi:10.1002/cne.901750203.

Rousseaux, M., Muller, P., Gahide, I., Mottin, Y., and Romon, M. (1996). Disorders of Smell, Taste, and Food Intake in a Patient With a Dorsomedial Thalamic Infarct. *Stroke* 27, 2328–2330. doi:10.1161/01.STR.27.12.2328.

Rovó, Z., Ulbert, I., and Acsády, L. (2012). Drivers of the Primate Thalamus. *J. Neurosci.* 32, 17894–17908. doi:10.1523/JNEUROSCI.2815-12.2012.

Salami, M., Itami, C., Tsumoto, T., and Kimura, F. (2003). Change of conduction velocity by regional myelination yields constant latency irrespective of distance between thalamus and cortex. *Proc. Natl. Acad. Sci.* 100, 6174–6179. doi:10.1073/pnas.0937380100.

Sapolsky, R. M., and Eichenbaum, H. (1980). Thalamocortical Mechanisms in Odor-Guided Behavior. *Brain. Behav. Evol.* 17, 276–290. doi:10.1159/000121804.

Schindelin, J., Arganda-Carreras, I., Frise, E., Kaynig, V., Longair, M., Pietzsch, T., et al. (2012). Fiji: an open-source platform for biological-image analysis. *Nat. Methods* 9, 676–682. doi:10.1038/nmeth.2019.

Schmitz, D., Schuchmann, S., Fisahn, A., Draguhn, A., Buhl, E. H., Petrasch-Parwez, E., et al. (2001). Axo-Axonal Coupling: A Novel Mechanism for Ultrafast Neuronal Communication. *Neuron* 31, 831–840. doi:10.1016/S0896-6273(01)00410-X.

Schneggenburger, R., Meyer, A. C., and Neher, E. (1999). Released Fraction and Total Size of a Pool of Immediately Available Transmitter Quanta at a Calyx Synapse. *Neuron* 23, 399–409. doi:10.1016/S0896-6273(00)80789-8.

Schwartz, M. L., Dekker, J. J., and Goldman-Rakic, P. S. (1991). Dual mode of corticothalamic synaptic termination in the mediodorsal nucleus of the rhesus monkey. *J. Comp. Neurol.* 309, 289–304. doi:10.1002/cne.903090302.

Seol, M., and Kuner, T. (2015). Ionotropic glutamate receptor GluA4 and T-type calcium channel Cav3.1 subunits control key aspects of synaptic transmission at the mouse L5B-POm giant synapse. *Eur. J. Neurosci.*, n/a–n/a. doi:10.1111/ejn.13084.

- References -

Sherman, S. M. (2001). Tonic and burst firing: dual modes of thalamocortical relay. *Trends Neurosci.* 24, 122–126. doi:10.1016/S0166-2236(00)01714-8.

Sherman, S. M. (2005). "Thalamic relays and cortical functioning," in Cortical Function: a View from the Thalamus., ed. B.-P. in B. Research (Elsevier), 107–126. Available at: http://www.sciencedirect.com/science/article/pii/S0079612305490093 [Accessed November 12, 2015].

Sherman, S. M., and Guillery, R. W. (2002). The role of the thalamus in the flow of information to the cortex. *Philos. Trans. R. Soc. B Biol. Sci.* 357, 1695–1708. doi:10.1098/rstb.2002.1161.

Sherman, S. M., and Guillery, R. W. (2006). *Exploring the thalamus and its role in cortical function*. 2nd ed. Cambridge, Mass: MIT Press.

Sherman, S. M., and Guillery, R. W. (2011). Distinct functions for direct and transthalamic corticocortical connections. *J. Neurophysiol.* 106, 1068–1077. doi:10.1152/jn.00429.2011.

Sincich, L. C., Adams, D. L., Economides, J. R., and Horton, J. C. (2007). Transmission of Spike Trains at the Retinogeniculate Synapse. *J. Neurosci.* 27, 2683 –2692. doi:10.1523/JNEUROSCI.5077-06.2007.

Slotnick, B. M., and Kaneko, N. (1981). Role of mediodorsal thalamic nucleus in olfactory discrimination learning in rats. *Science* 214, 91–92. doi:10.1126/science.7280684.

Slotnick, B. M., and Risser, J. M. (1990). Odor memory and odor learning in rats with lesions of the lateral olfactory tract and mediodorsal thalamic nucleus. *Brain Res.* 529, 23–29. doi:10.1016/0006-8993(90)90807-N.

Smith, P. G., and Marzban, F. (1998). Parasympathetic varicosity proliferation and synaptogenesis in rat eyelid smooth muscle after sympathectomy. *Brain Res.* 786, 171–180. doi:10.1016/S0006-8993(97)01439-X.

Špaček, J., and Lieberman, A. R. (1974). Ultrastructure and three-dimensional organization of synaptic glomeruli in rat somatosensory thalamus. *J. Anat.* 117, 487–516.

Staubli, U., Schottler, F., and Nejat-Bina, D. (1987). Role of dorsomedial thalamic nucleus and piriform cortex in processing olfactory information. *Behav. Brain Res.* 25, 117–129. doi:10.1016/0166-4328(87)90005-2.

Suzuki, S., and Rogawski, M. A. (1989). T-type calcium channels mediate the transition between tonic and phasic firing in thalamic neurons. *Proc. Natl. Acad. Sci.* 86, 7228–7232.

Talley, E. M., Cribbs, L. L., Lee, J.-H., Daud, A., Perez-Reyes, E., and Bayliss, D. A. (1999). Differential Distribution of Three Members of a Gene Family Encoding Low Voltage-Activated (T-Type) Calcium Channels. *J. Neurosci.* 19, 1895–1911.

Tham, W. W. P., Stevenson, R. J., and Miller, L. A. (2011). The impact of mediodorsal thalamic lesions on olfactory attention and flavor perception. *Brain Cogn.* 77, 71–79. doi:10.1016/j.bandc.2011.05.008.

Theyel, B. B., Llano, D. A., and Sherman, S. M. (2010). The corticothalamocortical circuit drives higher-order cortex in the mouse. *Nat. Neurosci.* 13, 84–88. doi:10.1038/nn.2449.

Traub, R. D., Schmitz, D., Jefferys, J. G. R., and Draguhn, A. (1999). High-frequency population oscillations are predicted to occur in hippocampal pyramidal neuronal networks

interconnected by axoaxonal gap junctions. *Neuroscience* 92, 407–426. doi:10.1016/S0306-4522(98)00755-6.

Turner, J. P., and Salt, T. E. (1998). Characterization of sensory and corticothalamic excitatory inputs to rat thalamocortical neurones in vitro. *J. Physiol.* 510, 829–843. doi:10.1111/j.1469-7793.1998.829bj.x.

Urra Quiroz, F. J. (2014). Giant Synapses in Thalamic Relay Cells.

Wang, X., and Sun, Q.-Q. (2012). Characterization of axo-axonic synapses in the piriform cortex of Mus musculus. *J. Comp. Neurol.* 520, 832–847. doi:10.1002/cne.22792.

Weyand, T. G., Boudreaux, M., and Guido, W. (2001). Burst and Tonic Response Modes in Thalamic Neurons During Sleep and Wakefulness. *J. Neurophysiol.* 85, 1107–1118.

Williams, S. R., and Mitchell, S. J. (2008). Direct measurement of somatic voltage clamp errors in central neurons. *Nat. Neurosci.* 11, 790–798. doi:10.1038/nn.2137.

Yarita, H., Iino, M., Tanabe, T., Kogure, S., and Takagi, S. F. (1980). A transthalamic olfactory pathway to orbitofrontal cortex in the monkey. *J. Neurophysiol.* 43, 69–85.

Yin, H. H., Adermark, L., and Lovinger, D. M. (2008). Neurotensin reduces glutamatergic transmission in the dorsolateral striatum via retrograde endocannabinoid signaling. *Neuropharmacology* 54, 79–86. doi:10.1016/j.neuropharm.2007.06.004.

Young, W. S., Alheid, G. F., and Heimer, L. (1984). The ventral pallidal projection to the mediodorsal thalamus: a study with fluorescent retrograde tracers and immunohistofluorescence. *J. Neurosci.* 4, 1626–1638.